Geophysical Journal International

Geophys. J. Int. (2017) **208,** 491–507
Advance Access publication 2016 October 14
GJI Geodynamics and tectonics

doi: 10.1093/gji/ggw392

The effect of a power-law mantle viscosity on trench retreat rate

Adam F. Holt[1,*] and Thorsten W. Becker[2]

[1]*Department of Earth Sciences, University of Southern California, Los Angeles, CA* 90089, *USA. E-mail: adamholt@mit.edu*
[2]*Jackson School of Geosciences, The University of Texas, Austin, TX* 78758, *USA*

Accepted 2016 October 13. Received 2016 September 21; in original form 2016 May 3

SUMMARY

The subduction of lithospheric plates is partitioned between subducting plate motion and lateral slab migration (i.e. trench retreat and advance). We use 3-D, dynamic models of subduction to address the role of a power-law mantle viscosity on subduction dynamics and, in particular, rates of trench retreat. For all numerical models tested, we find that a power-law rheology results in reduced rates of trench retreat, and elevated slab dip angles, relative to the equivalent isoviscous mantle model. We analyse the asthenospheric pressure distribution and the style of mantle flow, which exhibits only limited variability as a function of mantle rheology, in order to compute estimates of the mantle forces associated with subduction. The inclusion of a power-law rheology reduces the mantle shear force (which resists subducting plate motion) to a greater degree than it reduces the dynamic pressure gradient across the slab (which resists trench retreat). Therefore, the inclusion of a power-law mantle rheology favours a shift towards a subduction mode with a reduced trench retreat component, typically a relative reduction of order 25 per cent in our 3-D models. We suggest that this mechanism may be of importance for reducing the high trench retreat rates observed in many previous models to levels more in line with the average subduction partitioning observed on Earth at present (i.e. trench velocity $\leq$ plate velocity), for most absolute plate motion reference frames.

Key words: Mantle processes; Subduction zone processes; Dynamics of lithosphere and mantle; Rheology: mantle.

1 INTRODUCTION

The subduction of negatively buoyant slabs constitutes the primary driving force of plate tectonics (e.g. Jacoby 1973; Forsyth & Uyeda 1975). In addition to subducting plate (SP) motion, subduction can also occur via lateral migration of the SP hinge/trench, in a deep mantle, absolute plate motion (APM) reference frame. Lateral slab migration typically occurs in the SP direction, that is, 'slab roll-back' or 'trench retreat', but advancing trench motion towards the overriding plate (OP) also occurs at a limited number of trenches (e.g. Elsasser 1971; Carlson & Melia 1984; Jarrard 1986). While the choice of absolute reference frame complicates the deduction of trench migration rates and directions (e.g. Heuret & Lallemand 2005; Funiciello *et al.* 2008; Lallemand *et al.* 2008; Schellart *et al.* 2008; Becker *et al.* 2015), trench migration rates (V_T) are, on average, less than ~50 per cent of total convergence rates (V_C), albeit with large spread (e.g. Schellart *et al.* 2008; Becker & Faccenna 2009). SP motion (V_P) accommodates the remainder of the subduction rate, that is, $V_C = V_P + V_T$. The rates and direction of trench motions have direct consequences for the style of back arc deformation (e.g. Uyeda & Kanamori 1979; Lallemand & Heuret 2005), and understanding 'typical' V_T / V_C ratios is a prerequisite for using them to constrain plate reconstructions, including their APM component (e.g. Williams *et al.* 2015).

Numerical and analogue subduction models, within which the trench migrates self-consistently (i.e. 'dynamic models'), have been used extensively to explore the mechanical controls on SP kinematics. The total convergence velocity can, to first order, be predicted by considering the interplay of the slab pull driving force and the resisting forces associated with slab bending and mantle drag (e.g. Conrad & Hager 1999; Bellahsen *et al.* 2005). However, what dictates how convergence partitions between SP, V_P, and trench motion, V_T, remains difficult to isolate. Modelling studies have typically focused on isolated subducting slabs, neglecting the effect of an OP. These studies highlight, in particular, the strong control of slab strength on V_T (e.g. Enns *et al.* 2005; Bellahsen *et al.* 2005; Di Giuseppe *et al.* 2008; Funiciello *et al.* 2008; Faccenna *et al.* 2009). In addition to being consistent with observations relating to plate flexure (Billen & Gurnis 2005), plate–mantle viscosity contrasts of 100–1000 are generally required to produce both the variability in trench migration regimes, and average subduction partitioning (i.e. typically $V_T \leq V_P$) inferred to occur on Earth (e.g. Schellart 2004; Funiciello *et al.* 2008; Becker & Faccenna 2009). However, even for slabs within this intermediate strength range, single slab studies often appear to favour trench motion over plate motion, to a greater degree than that observed on

* Now at: Department of Earth, Atmospheric and Planetary Science, MIT, Cambridge, MA 02139, USA.

Earth (e.g. Funiciello *et al.* 2003; Stegman *et al.* 2006; Schellart *et al.* 2007).

For a given slab strength, a significant trench retreat reducing feature of the subduction system appears to be the presence of an OP. Dynamic models that incorporate an OP are now routinely studied in 2-D (e.g., Capitanio *et al.* 2010; Sharples *et al.* 2014; Garel *et al.* 2014; Holt *et al.* 2015a; Petersen *et al.* 2015), and increasingly so in 3-D (e.g., Yamato *et al.* 2009; Duarte *et al.* 2013; Schellart & Moresi 2013; Jagoutz *et al.* 2015). The presence of an OP modifies the force balance acting on the SP, which shifts subduction partitioning toward SP motion, that is, reducing V_T / V_P (Yamato *et al.* 2009; Butterworth *et al.* 2012; Holt *et al.* 2015a). Additionally, in 3-D, the width of the trench has been shown to exert a significant control on rates of trench retreat, with wide trenches typically exhibiting reduced rates in numerical models, and on Earth (e.g. Dvorkin *et al.* 1993; Stegman *et al.* 2006; Schellart *et al.* 2007; Stegman *et al.* 2010). Here, we focus on the role that a stress-dependent mantle rheology, a feature typically neglected in dynamic subduction models, has on the partitioning of subduction between V_T and V_P.

The 3-D modelling studies discussed above typically consider a uniform viscosity mantle, and so neglect the role of lateral viscosity variations in the sublithospheric mantle. Laboratory experiments, however, predict that deformation in large regions of the upper mantle is dominated by dislocation creep, in which the effective viscosity has a power-law dependence on stress (e.g., Karato & Wu 1993; Hirth & Kohlstedt 2003). Furthermore, seismic anisotropy observed in the upper mantle can likely be attributed to dislocation creep deformation, which generates lattice preferred orientations in olivine (e.g. Nicolas & Christensen 1987). Analyses which combine observations of seismic anisotropy with global, or regional, flow computations suggest that flow in the oceanic mantle is dominated by dislocation creep between depths of ∼100 and 400 km (e.g. Podolefsky *et al.* 2004; Becker 2006; Behn *et al.* 2009). 2-D numerical models show that the inclusion of a stress-dependent rheology decreases the mantle wedge viscosity, which reduces the hydrodynamic stresses on the upper surface of the slab, thereby resulting in an increased slab dip angle (Tovish *et al.* 1978; Billen & Hirth 2005, 2007). However, these models fix the trench location and so uncertainty remains regarding whether variations in trench rollback rate, which exert a first order control on slab dip (e.g. Christensen 1996), would counteract this dip-increasing effect. A number of 2-D, numerical models that do allow the trench to move freely have been used investigate how the slab rheology influences slab kinematics and slab-interaction with a more viscous lower mantle (e.g., Androvičová *et al.* 2013; Čížková & Bina 2013; Garel *et al.* 2014; Holt *et al.* 2015a), but the role of a stress-dependent mantle viscosity on trench rollback has not, to our knowledge, been explicitly considered in a dynamic framework. While relative reductions in mantle viscosity triggered by a stress-dependent viscosity intuitively result in elevated slab sinking rates, and greater subduction-induced mantle flow velocities (e.g. Jadamec & Billen 2012; Billen & Jadamec 2012), the degree to which such localized weakening shifts the convergence partitioning between V_T and V_P is not clear.

Coupled to the subduction kinematics is the style of subduction-induced mantle flow. Subduction excites poloidal flow in the vertical plane and, in 3-D, toroidal flow. Return flow associated with a near-stationary trench is dominantly poloidal, whereas horizontal motion of a subducting slab, in the form of trench retreat or advance, promotes toroidal flow around the slab edges (e.g., Dvorkin *et al.* 1993; Buttles & Olson 1998; Kincaid & Griffiths 2003; Funiciello *et al.* 2003, 2004; Schellart 2004; Stegman *et al.* 2006; Piromallo *et al.* 2006). Understanding the dynamic controls on the style of subduction-induced return flow is important both in aiding the interpretation of shear-wave splitting measurements which can probe horizontal/subhorizontal mantle flow (e.g. Long & Becker 2010), constraining the mantle pressure field and the intertwined slab kinematics (e.g. Royden & Husson 2006), and understanding the locations of off-axis volcanoes associated with subduction-induced upwelling flow (e.g. Faccenna *et al.* 2010). Therefore, we also analyse the mantle flow regime in our numerical models. After characterizing how the presence of an OP affects mantle flow in a dynamically evolving subduction setting, as previously considered for 3-D numerical models which prescribe slab kinematics (Honda 2009), we assess whether the inclusion of a power-law mantle rheology modifies the style of subduction-induced mantle return flow.

2 METHODOLOGY

We use the finite-element code CitcomCU (Moresi & Gurnis 1996; Zhong 2006) to construct numerical, time-evolving subduction models in both (pseudo) 2-D and 3-D domains. CitcomCU solves the conservation equations which govern convection in an incompressible viscous fluid (Boussinesq approximation) with negligible inertia. Our models solve for the conservation of energy, mass (continuity eq.), and momentum (Stokes eq.), but we neglect thermal diffusion (see Section 2.1). 2-D models are less computationally expensive and so allow us to initially probe the parameter space more extensively in order to inform our 3-D model parameters, as well as examine the role of lithospheric viscoplasticity. 3-D models are then used to verify the applicability of the 2-D model systematics to subduction systems with finite width trenches. In addition to plate kinematics, the 3-D models are used to investigate the dynamic evolution of both the mantle flow and viscosity fields. The mechanical and rheological parameters are equivalent for the two suites of models which initiate with a deep initial slab (see Fig. 1 and Table 1). Numerically, the only differences are that the 2-D models contain only one finite element in the third, y-dimension (e.g. Holt *et al.* 2015b), while 3-D models contain many elements (256) in order to resolve a finite width trench and a passive side plate. That aside, the two models contain the same sized and number of finite elements in the vertical plane. Our explanation of the 3-D model setup in the next section is therefore also applicable to the 2-D models presented in section 3.1.

2.1 Numerical model setup

In order to target the first order effects of a power-law rheology on slab dynamics, we use a simplified geometrical, mechanical, and rheological setup. We consider two active plates, an SP and an OP, and a passive side plate which is separated from the subduction system plates by 25 km of mantle material. The side plate, while not participating directly in subduction, prevents rapid plate shortening in the trench parallel direction, and spontaneous subduction along the edge of the SP. Without the side plate, such unphysical effects occur due to the lateral juxtaposition of dense lithosphere with light mantle, a configuration not expected to occur on Earth (e.g. Yamato *et al.* 2009). The side plate also provides a convenient reference frame for velocities measured in the subduction systems (e.g. trench retreat rates). The trench-perpendicular lengths of the SP and OP exert a strong control on rollback rates, and so we examine variable plate lengths, relative to the vertical (upper mantle) dimension of 660 km, to assess the effect of a power-law viscosity on models with a wide range of slab kinematics.

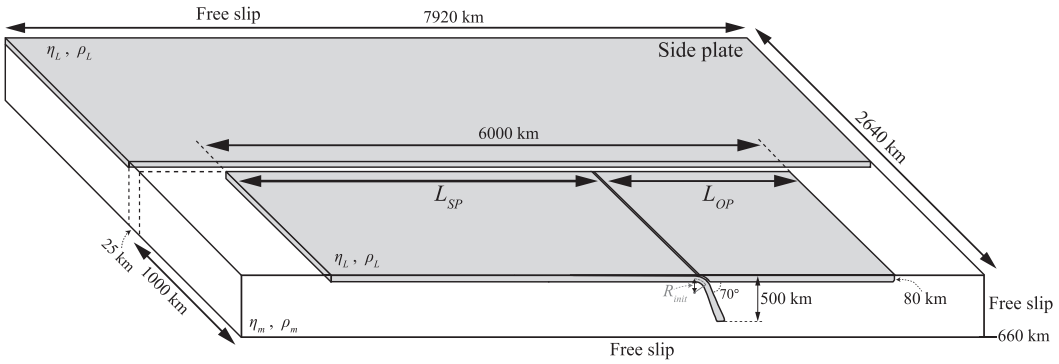

Figure 1. Schematic illustration of the initial conditions for the 3-D numerical models. The 2-D numerical models have an equivalent setup but neglect the *y*-dimension (i.e. dimension with length = 2640 km).

Table 1. Numerical model parameters.

Symbol	Parameter	Value	Units
	Geometry		
h	Domain height (z)	660	km
l	Domain length (x)	7920	km
w	Domain width (y)	5280	km
w_T	Trench width	2000	km
h_{lith}	Lithospheric thickness	80	km
h_{crust}	Crustal thickness	15	km
L_{SP}	Subducting plate length	2000, 3000, 4000	km
L_{OP}	Overriding plate length	2000, 3000, 4000	km
R_{init}	Initial radius of curvature	150	km
z_{notch}	Initial slab depth	150, 500	km
θ_{init}	Initial slab dip angle	70°	–
	Mechanical and rheological properties		
ρ_0	Mantle density	3300	kg m^{-3}
$\Delta\rho$	Plate-mantle density contrast	85	kg m^{-3}
η_{lith}	Lithosphere viscosity	1.4×10^{23}	Pa s
η_{crust}	Crust viscosity	2.8×10^{20}	Pa s
η^N_{mantle}	Newtonian, mantle viscosity	2.8×10^{20}	Pa s
n	Power-law exponent	3.5	–
$\dot{\varepsilon}^T_{\text{II}}$	Transition strain rate	10^{-15}, 5×10^{-15}, 10^{-14}, 10^{-13}	s^{-1}

We simplify our model setup by neglecting thermal diffusion (e.g. Enns *et al.* 2005), thereby considering a density and viscosity field that is dependent purely on composition, which is advected using tracer particles (McNamara & Zhong 2004). The effect of thermal diffusion to disperse slabs is dependent on the local Peclet number, which is typically large. Thermal slabs are therefore expected to be fairly coherent in the lower mantle (e.g. Tan *et al.* 2002), and so we consider this a reasonable simplification to enable extraction of the core physical processes. The domain size is 7920 km (length, x) $\times$ 660 km (height, z) $\times$ 5280 km (width, y), and all boundaries are mechanically free slip. We initially place 40 tracers within each of the elements, which are used to define the lithospheric plates, and the weak 'crustal' layer that decouples the lithospheric plates. The finite element dimensions are 6 km in regions which are both in the upper 200 km of the domain, and within a 1500 km widge (x-direction) region centred around the trench. Elsewhere, finite elements have dimensions of $\approx$14 km. A free-slip boundary condition may render the slab tip overly mobile atop the upper-lower mantle boundary, and so we additionally test the effect of a no-slip lower boundary which approximates a high viscosity lower mantle.

We consider plates with widths of 2000 km. For each of the 3-D models, we take advantage of the plate symmetry about $y = 0$ (i.e. trench-perpendicular horizontal axis), which enables us to half the computational domain (i.e. $y = 2640$ km). Lithospheric plates have a constant density contrast, relative to the sublithospheric mantle, of 85 kg m^{-3} and a constant thickness of 80 km. The sublithospheric mantle has a reference density of 3300 kg m^{-3}. Subduction is initiated by allowing the SP to extend below the OP with a centre-line radius of curvature (R_{init}) of 150 km. The centre-line is the line which is equidistant from the two surfaces of the SP (Fig. 1). Below the curved portion of the initial lithospheric geometry, we allow the plate to extend to a depth of 500 km with an initial dip angle of 70°. The initial, deep placement of the slab-tip near the model base results in a suite of models which have a consistent style of evolution, with all slabs bending backward on top of the impermeable base of the domain, as opposed to slabs which bend forward and roll over the lower boundary. While this initial condition reduces the observed variability in slab kinematics, it allows us to focus on the subduction mode which appears most akin to subduction on Earth. Otherwise, much of the kinematic variability after slab interaction with the model base is a direct result of the different styles of slab bending. However, for the 2-D models, we do examine a suite of models in which the initial slab is restricted to shallow depths of $<$150 km.

2.1.1 *Rheology*

We use a composite Newtonian (diffusion creep) and power-law (dislocation creep) rheology (e.g. Zhong *et al.* 1998). Due to the compositional nature of our models, we neglect the temperature

dependence of viscosity, and additionally omit the pressure dependence. As reviewed recently by King (2016), there remains significant uncertainty regarding the appropriate creep law parameters, even for the dominant upper mantle mineral, olivine. Additionally, grain size, which exerts a strong control on the relative dominance of diffusion and dislocation creep, is likely both spatially variable and time-dependent. Given such uncertainties, we therefore chose a simplified rheological parameterization, which enables us to isolate first order dynamic effects, and ensures relatively easy reproducibility. However, the depth-extent of power-law viscosity dominance in our models is broadly consistent with the ∼100–400 km inferred from studies which incorporate seismic anisotropy (e.g. Podolefsky *et al.* 2004; Becker 2006; Behn *et al.* 2009), which gives us confidence in the applicability of our rheological approach to Earth.

Our effective viscosity is composed of an isoviscous Newtonian component, η^N, and a power-law component, η^P, and is computed as,

$$\eta^{\text{eff}} = \frac{\eta^N \eta^P}{\eta^N + \eta^P} = \left(\frac{1}{\eta^N} + \frac{1}{\eta^P} \right)^{-1}. \quad (1)$$

The Newtonian viscosity component in the asthenospheric mantle (η^N_{mantle}) is 2.8×10^{20} Pa s, and lithospheric plates are a factor 500 stronger than the Newtonian mantle component (i.e. $\eta^N_{\text{lith}} = 1.4 \times 10^{23}$), in line with the constraints outlined in the introduction. We impose a minimum effective viscosity cut-off of 2.8×10^{18} Pa s (i.e. $0.01 \times 10^{-2} \eta^N_{\text{mantle}}$). We have tested a lower viscosity cut-off of $0.0001 \times 10^{-4} \eta^N_{\text{mantle}}$ for our most non-linear 2-D models, and find that the results are near identical, that is, plate velocities differ within a single per cent, and model behaviour is consistent. This viscosity formulation constitutes two dashpots in series, that is, $\dot{\varepsilon}^{\text{total}}_{\text{II}} = \dot{\varepsilon}^N_{\text{II}} + \dot{\varepsilon}^P_{\text{II}}$, where $\dot{\varepsilon}_{\text{II}} = \sqrt{\dot{\varepsilon}_{ij}\dot{\varepsilon}_{ij}/2}$ is the second invariant of the deviatoric strain rate (Einstein summation convention). The power-law viscosity component is given by

$$\eta^P = \eta^N \left(\frac{\dot{\epsilon}_{\text{II}}}{\dot{\epsilon}^T_{\text{II}}} \right)^{\frac{1-n}{n}}, \quad (2)$$

where n is the power-law exponent (= 3.5), and $\dot{\varepsilon}^T_{\text{II}}$ is the transition strain rate. Due to the strain-rate dependence of viscosity, we iteratively solve Stokes equation until the global change in velocity, normalized by the absolute velocity, is below 0.01. For the 2-D case, we have verified that a stricter, power-law convergence criterion of 0.001 does not affect the model results. $\dot{\varepsilon}^T_{\text{II}}$ is the strain rate at which the Newtonian and power-law components are equal (i.e. $\dot{\varepsilon}^N_{\text{II}} = \dot{\varepsilon}^P_{\text{II}}$). We therefore focus on the effect of varying $\dot{\varepsilon}^T_{\text{II}}$ which controls the proportion of the domain within the power-law deformational regime. Because strain rates are significantly larger in the flowing mantle than in the lithospheric plates, power-law deformation is focussed into the sublithospheric mantle. Such power-law focussing is consistent with a number of modelling studies that include laboratory derived olivine creep laws (e.g. Billen & Hirth 2005, 2007; Čížková & Bina 2013).

In the 2-D suite of models, we additionally test the effect of viscoplastic yielding. In this case, an additional viscosity component, η^{yield}, is computed from a prescribed yield stress, τ^{yield}, as follows (e.g. Schott & Schmeling 1998),

$$\eta^{\text{yield}} = \frac{\tau^{\text{yield}}}{2\dot{\varepsilon}_{\text{II}}}, \quad (3)$$

with a Byerlee (1968) type yield stress, $\tau^{\text{yield}} = (a\sigma_l + b)\lambda$. a is the friction coefficient (0.6), b is the cohesion (60 MPa), σ_l is the lithostatic pressure, and λ is a constant, 'pore pressure' prefactor (0.15), with a value comparable to that used in previous studies (e.g. Enns *et al.* 2005: 0.1; Di Giuseppe *et al.* 2008: 0.08). η^{yield} is then added as another component in the harmonic mean expression for η^{eff} (eq. 1). To properly characterize the impact of varying extents of lithospheric weakening, we have also examined models with variable yield stresses for our intermediate transition strain rate model ($\dot{\varepsilon}^T_{\text{II}} = 5 \times 10^{-15}$ s^{-1}): We consider plates with a range of depth-dependent yield stresses ($\lambda = 0.1$–0.2), and a range of constant yield stresses ($\tau^{\text{yield}} = 100$–$1000$ MPa).

To facilitate decoupling of the SP from the OP, we insert a 15 km thick, weak (= η^N_{mantle}) crustal layer within SP (e.g. Běhounková & Čížková 2008). The crust, defined by compositional tracers, is linearly tapered from full thickness at a depth of 200 km (and above), to zero thickness below a depth of 400 km, in order to avoid stress discontinuities. For more details about the implementation of the compositional crust, and resolution tests for similar 2-D numerical models, see Holt *et al.* (2015a).

3 RESULTS

3.1 2-D Models

We now consider the effect of a power-law mantle on 2-D slabs, which are, by definition, equivalent to slabs with infinite width trenches. Numerical models which are initiated by a shallow proto-slab are shown in Fig. 2. Decreasing the transition state increases the proportion of the asthenosphere deforming dominantly in the power-law viscosity regime (i.e. eq. 2). As expected, power-law deformation is focused in the portions of the asthenosphere next to the slab and surface plates (e.g. Billen & Hirth 2007; Garel *et al.* 2014). Here, high strain rates result from the shearing of the adjacent asthenosphere by the mobile plates/slab. Additional regions that undergo more moderate, power-law deformation are the return-flow upwellings that occur below the trailing edge of the SP, and above the slab tip. For a transition strain rate of 10^{-15} s^{-1}, effective viscosities are in some places reduced by over an order of magnitude, particularly directly adjacent to the subducting slab (Fig. 2e). For a transition strain rate of 10^{-14} s^{-1}, the more spatially limited power-law regions have viscosities reduced by a factor of ∼5, relative to the Newtonian viscosity component (Fig. 2c).

Fig. 2 shows the strong dependence of slab morphology, particularly slab dip angle, on the transition strain rate. As the transition strain rate decreases, that is, as the power-law viscosity component becomes more dominant, the slab dip angle gradually increases up until the slab bends forward over the model base for a transition strain rate of 10^{-15} s^{-1} (Fig. 2e). As discussed by Ribe (2010), whether the slab initially leans backwards or forwards at an impermeable model base is a function of the dip angle of the slab as it impinges on the boundary. For transition strain rates of 5×10^{-15} s^{-1} and greater, slabs impinge on the lower boundary with a dip angle $<90^\circ$, and so lean initially backwards on top of the lower boundary, while the opposite is true for a transition strain rate of 10^{-15} s^{-1}.

Additionally shown in Fig. 2 are mantle flow velocities. On average, the mantle flow becomes faster as the transition strain rate is reduced. To facilitate comparison of the mantle flow regime, we therefore use a Stokes velocity scaling ($V_{\text{Stokes}} \propto \Delta\rho g h^2_{\text{lith.}} / \langle\eta_{\text{mantle}}\rangle$) to normalize the mantle flow velocities by a reference velocity. Aside from mantle viscosity, the other V_{Stokes} components are held constant throughout this study, such that $\langle\eta_{\text{mantle}}\rangle$ values dictate our reference velocity, computed as $V_{\text{ref}} = C / \langle\eta_{\text{mantle}}\rangle$. We choose $\langle\eta_{\text{mantle}}\rangle$ to be the harmonic mean viscosity extracted from a sublithospheric,

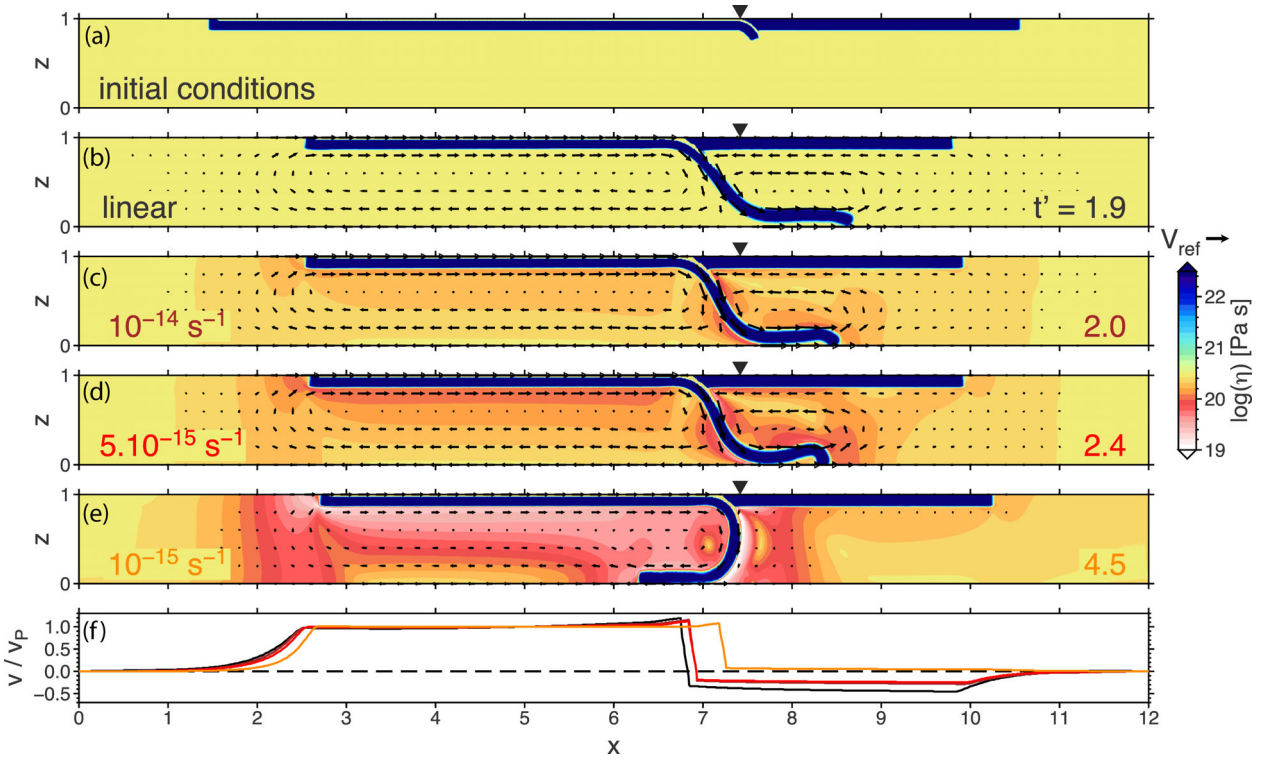

Figure 2. Viscosity field snapshots showing the suite of 2-D numerical models initiated with a shallow initial protoslab, at broadly equivalent time steps based on slab morphology. In addition to panels showing the models with variable transition strain rates, $\dot{\varepsilon}_{II}^{T}$ (c–e), the equivalent isoviscous mantle model (b), and initial conditions (a), are shown. Overlain are mantle velocity vectors normalized by a reference velocity, computed as described in the main text. The normalized model times (bottom right corner) are computed by dividing the dimensional times by a reference time ($t' = t / t_{ref} = tV_{ref} / h$). Inverted triangles indicate the initial trench location. The bottom panel, (f), compares the plate velocities, normalized by the average SP velocity.

vertical profile at a distance of 1000 km to the left of the trench. The reference velocity pre-factor, C, is set so that V_{ref} is equivalent to the convergence rate for the appropriate (i.e. 2-D or 3-D) reference, isoviscous mantle model. Similarly, dimensional time is normalized by a reference time (t_{ref} = 660 km/V_{ref}). Aside from the model where the slab bends over forwards ($\dot{\varepsilon}_{II}^{T} = 10^{-15}$ s^{-1}), the large-scale mantle flow patterns are similar for the models with variable degrees of power-law deformation.

In Fig. 2(f), we plot plate velocities. To highlight variability in OP velocity which, in the forearc region, is approximately equal to the trench velocity, we normalize the plate velocities by the average SP velocity. In addition to the increasing slab dip angle, the normalized trench velocity decreases as the power-law viscosity component becomes more dominant. For a transition strain rate of 10^{-15} s^{-1}, the trench is near-stationary. The stationary trench results in only minor asthenospheric flow beneath the OP, as the subducting slab is decoupled from the mantle wedge by the relative, effective viscosity reductions associated with the power-law viscosity component.

We also examine numerical models with initial conditions that result in an equivalent backwards-bending subduction mode for all of the rheologies considered, in order to make direct comparisons (Fig. 3). In these models, slab dip also increases as the transition strain rate decreases, and the increase in slab dip is coupled with a reduction in trench retreat velocity (Fig. 3f). For equivalent models times, and L_{SP} = 4000 km, Fig. 4 shows the variation of the slab dip angle, and the log of the trench retreat velocity (V_T) over the plate velocity (V_P), as a function of the transition strain rate. Relative to the reference model with an isoviscous mantle, the dip angle increases by ≈30° and $\log_{10}(V_T / V_P)$ decreases by ≈0.33 in the non-Newtonian model with the lowest transition strain rate (10^{-15} s^{-1}).

To verify the more general applicability of these results, we additionally examine suites of models with shorter initial SPs (L_{SP} = 2000 km) and plastic yielding (eq. 3: λ = 0.15). While reducing L_{SP} increases slab dip angle and reduces V_T / V_P, the basic trends are unchanged (Fig. 4). Similarly, the addition of plasticity (i.e. viscosity reduction in the bending region) does not change the trend observed, but increases the relative rate of trench motion. Thus, we show that the sense of variation in slab dip and trench retreat rate, as a function of mantle rheology, is equivalent for models with both plastic yielding and short SPs. Interpretation of the models which include plastic yielding is complicated by the feedback between yielding and the degree of power-law flow in the sublithospheric mantle. As the power-law transition strain rate is reduced and the mantle moves further into the power-law regime, slab bending stresses increase which, in turn, increases the extent of the SP hinge which yields. We expect that this behaviour is responsible for the slight decrease in V_T / V_P observed at high transition strain rates (Fig. 4b). Due to this complexity, we have additionally investigated a suite of models where we hold the mantle rheology constant (5×10^{-15} s^{-1} transition strain rate), and vary the yield stress for both Byerlee (λ = 0.1, 0.15, 0.2) and constant yield stress plasticity (τ^{yield} = 100, 200, 1000 MPa). We find that varying the yield stress results in changes in V_T / V_P that are of second order, relative to those induced by varying the transition strain rate. An exception occurs in the models which have yield stresses that are low enough to induce slab break-off (λ = 0.1 and τ^{yield} = 100 MPa). Here, slab break-off exerts a strong control on plate kinematics, but this is beyond the scope of this work which is focused on mature, sustained subduction.

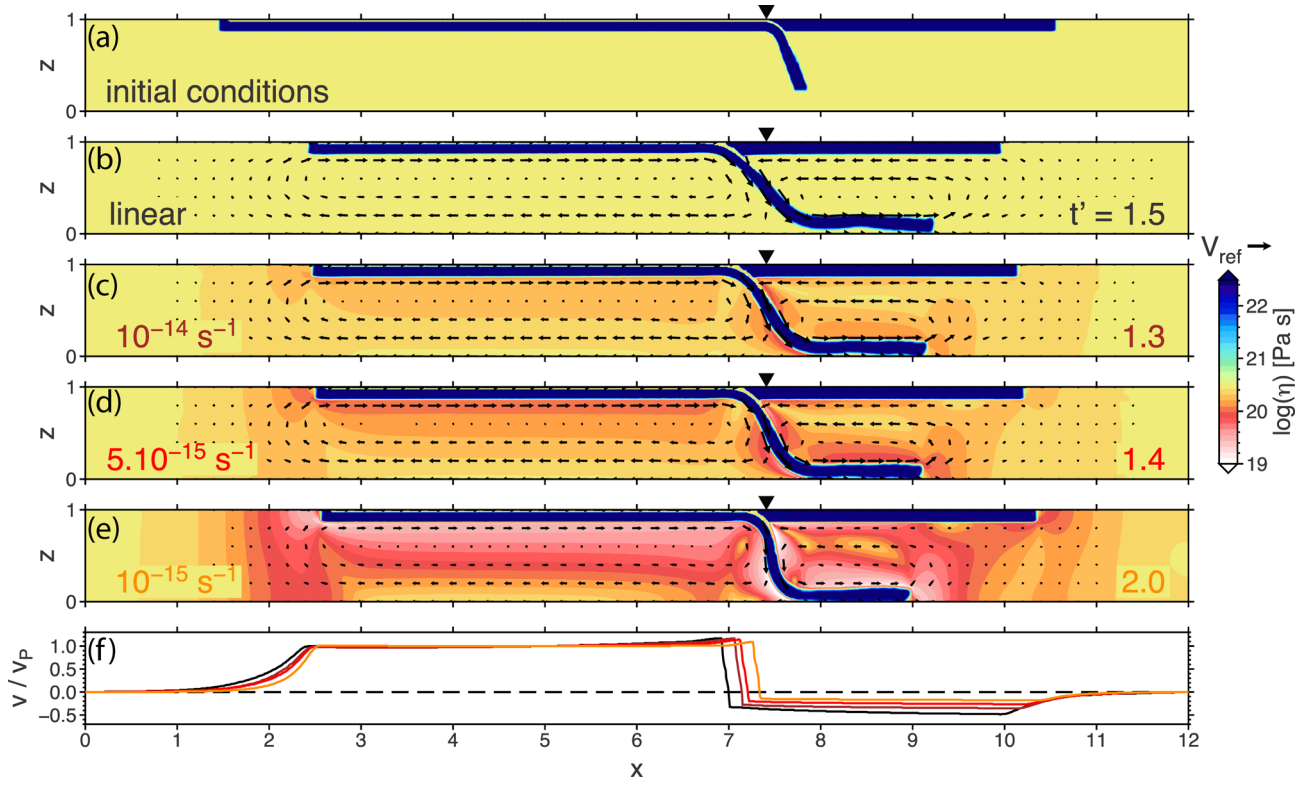

Figure 3. As in Fig. 2, but for the 2-D models with a deeper initial slab geometry.

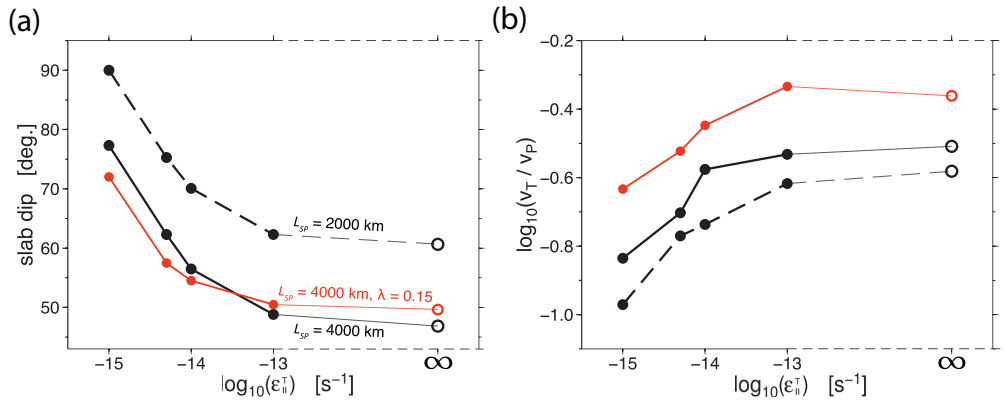

Figure 4. Plate kinematics as a function of transition strain rate for the 2-D models with deep initial slab geometry, extracted at time steps equivalent to those shown in Fig. 3. In addition to the long SP models shown in Fig. 3 (initial L_{SP} = 4000 km: black, solid lines), kinematics from short SP models (L_{SP} = 2000 km: black, dashed lines), and long SP models with plasticity (L_{SP} = 4000 km and $\lambda = 0.15$: red lines) are plotted. The plasticity suite of models are plotted at an earlier stage of subduction, but still after flattening on the model base, due to later-stage instability (i.e. OP subducts) for the lowest transition strain rate model. Shown is, (a), the average slab dip angle computed between depths of 200 and 460 km and, (b), the log of the ratio of trench retreat velocity and SP velocity. The kinematics extracted from the equivalent Newtonian models are placed at an arbitrary, 'infinite' transition strain rate x-location, for illustrative purposes.

3.2 3-D Models

We now present 3-D numerical models to explore whether the 2-D results are robust in 3-D. Additionally, we probe the effect that such a non-linear rheology has on 3-D mantle flow.

3.2.1 Model evolution

We analyse 3-D models with equivalent properties, and initial conditions, to the suite of 2-D models shown in Fig. 3. Fig. 5 shows the viscosity fields for models both with an isoviscous mantle, and with a composite power-law rheology ($\dot{\varepsilon}_{II}^{T} = 5 \times 10^{-15}$ s^{-1}). As in the 2-D models, the dip angle is elevated in the power-law models, and the power-law regime is active primarily in the portion of the asthenosphere being directly sheared by adjacent plates/slab. However, in the 3-D models, a significant portion of the subduction-induced mantle return flow occurs in the form of toroidal flow around the slab edge, which induces strain rates large enough (i.e. $>5 \times 10^{-15}$ s^{-1}) for deformation to occur within the power-law regime. We have additionally examined equivalent models where the OP is absent (Fig. 6), and where the base of the model has a no slip boundary condition (not shown). In the single slab experiments, the lack of an

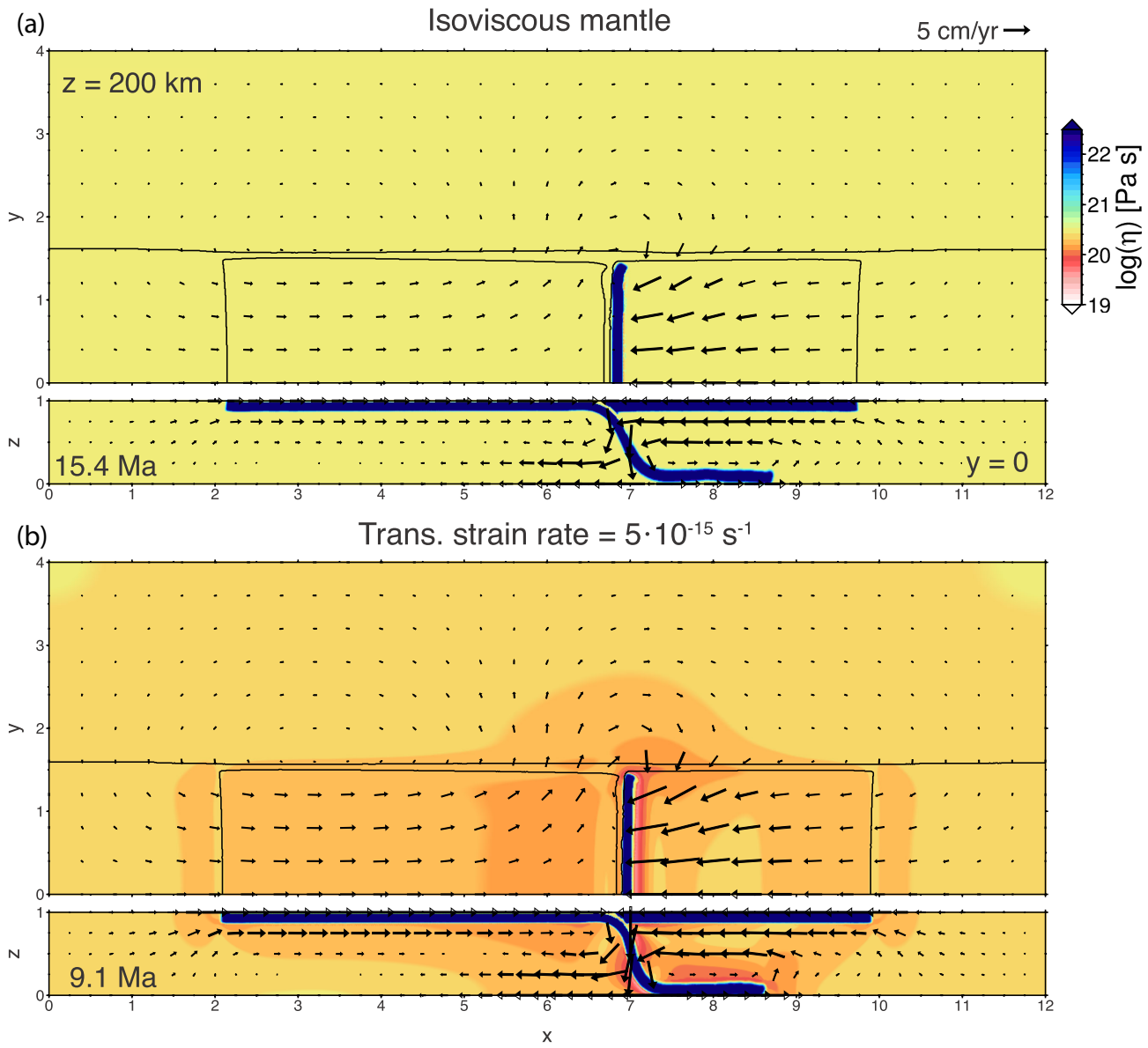

Figure 5. Comparison of viscosity and mantle flow fields for 3-D models (L_{SP} = 4000 km) with, (a), an isoviscous mantle and, (b), a composite power-law/Newtonian mantle rheology with a transition strain rate of 5×10^{-15} s^{-1}. Both models are plotted at broadly equivalent time steps based on slab morphology. For each model the upper panel shows a horizontal, sublithospheric slice ($z = 200$ km), and the lower panel shows a vertical slice through the model/plate mid-plane ($y = 0$). In the horizontal slices, the surface plate geometries are overlain in black.

OP promotes both the development of slab curvature and slab/trench rollback (e.g. Stegman *et al.* 2006; Schellart *et al.* 2007), relative to the models which include an OP. Therefore, power-law deformation associated with rollback-driven toroidal flow is greater in the single slab model (*cf.* Figs 5b and 6b). In the model with a no slip base, the subducting slab morphology is similar to that observed in the free slip models, but subduction rates are reduced by 30–40 per cent, and the size of regions dominated by power-law deformation is also reduced.

As for the 2-D cases, we consider models with variable initial SP lengths. While the power-law deformation is generally located preferentially below the SP, a shift towards more wide-spread power-law deformation below the OP occurs for greater L_{SP}. This occurs because as L_{SP} increases, the OP moves more rapidly due to trench retreat, which results in greater shear strain rates below the OP. Where power-law deformation occurs within the sublithospheric mantle dictates the spatial distribution of basal traction on the lithospheric plates which, in turn, dictates the overall effect of a power-law mantle on slab kinematics. This is discussed in detail in section 4.3.

3.2.2 3-D mantle flow

We now compare the 3-D mantle flow field for the long SP models with, and without, a power-law viscosity component ($\dot{\varepsilon}_{II}^{T} = 5 \times 10^{-15}$ s^{-1}). The vertical and horizontal mantle flow field, normalized as described in Section 3.1, is shown in Fig. 7. Prior to normalization, the average mantle flow velocity is ≈50 per cent greater in the power-law models, due to reduced average mantle viscosity. However, after normalizing, the flow patterns are again very similar for the two models. Similarly, for models both without an OP, and with no slip basal boundary conditions, we find that a

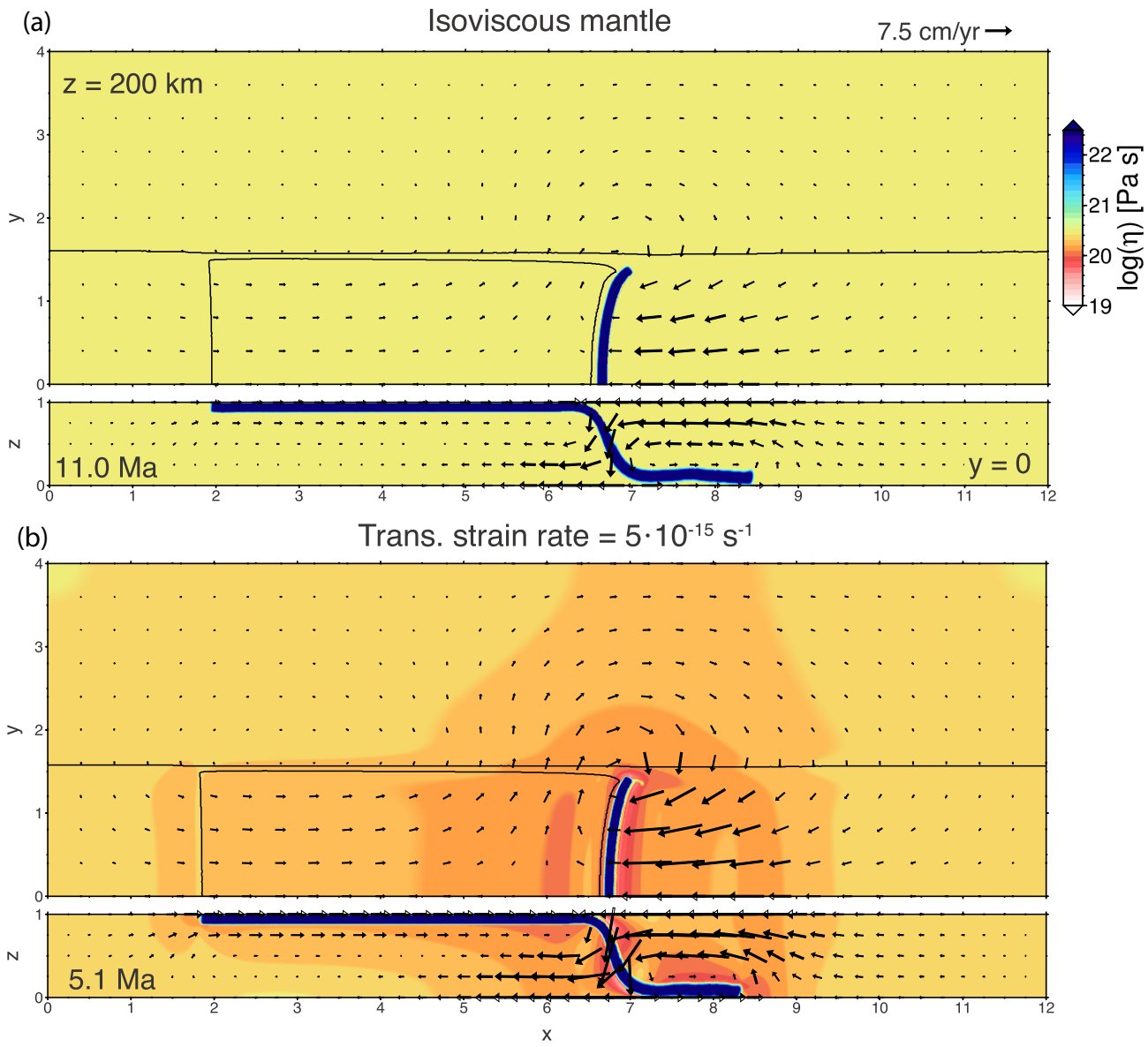

Figure 6. As in Fig. 5, but for the models without an OP.

power-law mantle rheology also exerts only a minor influence on the broad scale mantle flow pattern. As subduction is partitioned between trench retreat and SP advance in these models, return flow is partitioned between, respectively, toroidal flow around the slab edges and upwelling in the vertical plane. In all of the models explored, there are multiple regions with significant upwards-directed vertical mantle flow, the locations of which may have implications for the location of decompression melting-induced volcanism (e.g. Faccenna *et al.* 2010). In addition to upwelling flow at the trailing edges of the two plates, a vigorous mantle upwelling occurs at the lateral edge of the slab-tip, and more moderate vertical flow is associated with flow around the slab edge (i.e. subhorizontal toroidal flow cell).

In order to quantify the mantle flow characteristics, we examine the mantle flow partitioning between toroidal and poloidal components (e.g., Bercovici 1993). Following, for example, Tackley (2000), the 2-D velocities on each horizontal layer are decomposed into irrotational (i.e. poloidal) and divergence-free (i.e. toroidal) vector fields. The vertical velocity field is added to the poloidal field, and toroidal/poloidal ratio (TPR) is taken as the toroidal RMS velocity divided by the poloidal RMS velocity. We compute the RMS of the poloidal and toroidal velocity fields for 10 horizontal layers ($\Delta z = 66$ km), and plot vertical profiles of the horizontal RMS velocities in order to characterize both the role of an OP (Fig. 8), and a power-law mantle rheology (Fig. 9), on mantle flow partitioning.

We examine the flow field for our two plate length end-members, $L_{SP} = 2000$ and 4000 km (Fig. 8). As discussed, trench retreat is dominant in the $L_{SP} = 4000$ km model, for slabs both with and without OPs. This results in the dominance of trench retreat-induced toroidal flow (i.e. $\log_{10}(\mathrm{TPR}) > 0$) over a substantial depth range (200 km $< z <$ 460 km) (Fig. 8c). Toroidal flow around the slab edge is focused in the mid-upper mantle, while poloidal mantle flow is dominant only near both the surface and the model base (*cf.* Becker & Faccenna 2009; Fig. 10). In contrast, the shorter SP model exhibits dominantly poloidal flow at all depths (i.e. $\log_{10}(\mathrm{TPR}) < 0$). The absence of an OP enhances the relative importance of trench retreat, thereby increasing TPR at mid-mantle depths. This effect is

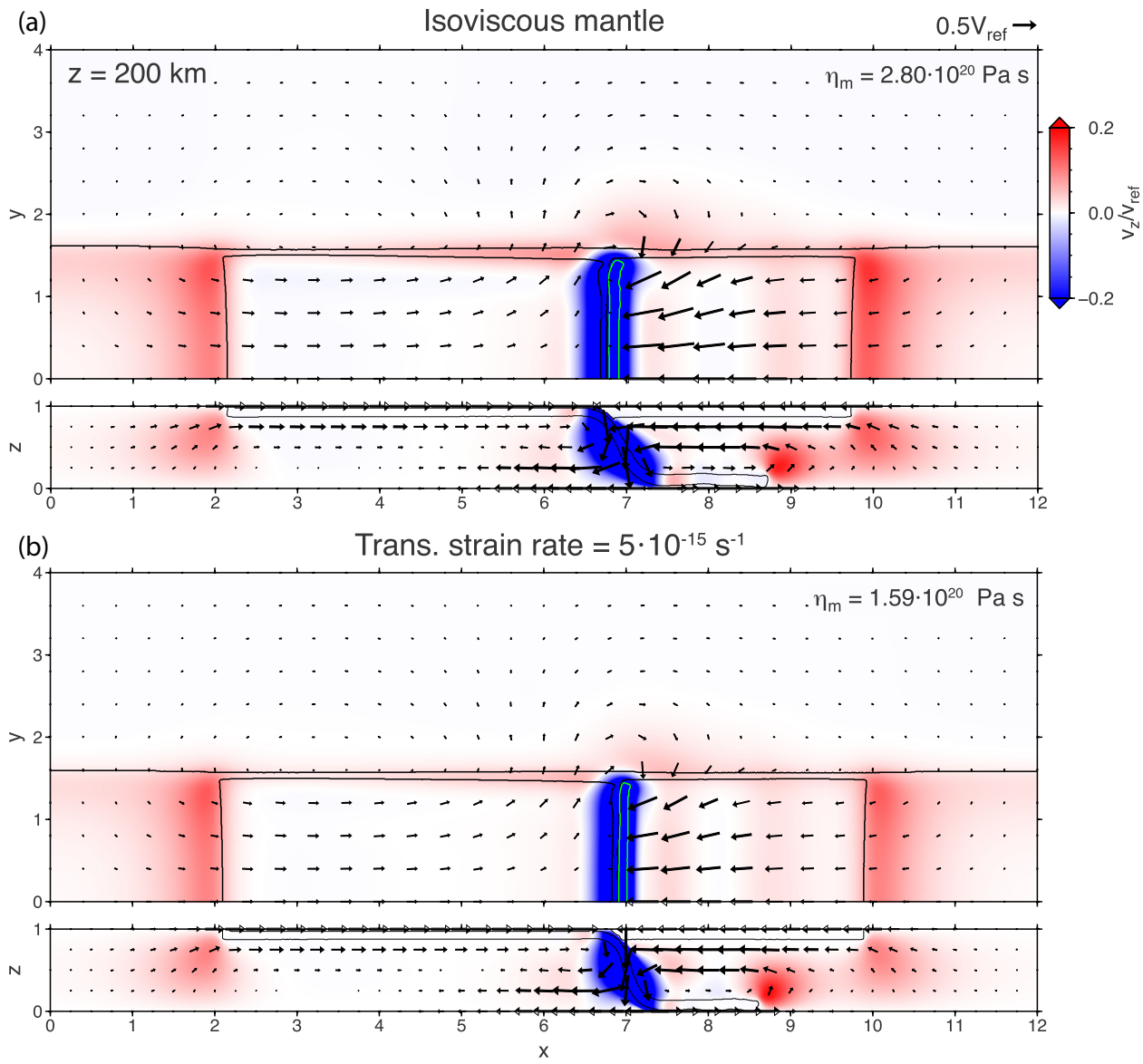

Figure 7. Non-dimensional mantle velocity field for the models shown in Fig. 5. Velocities are normalized by a reference velocity computed using an average sublithospheric viscosity (shown in top-right corner), taken from a sublithospheric profile at 750 km to the left of the trench. For each model, the top panels show the vertical velocity extracted at a depth of 200 km, overlain by the mantle velocity vectors. The lower panels show the vertical velocity field plotted in the vertical plane, at $y = 0$.

particularly prominent for the short SP case, in which the absence of a large OP exerts a stronger effect on slab dynamics than in the long SP models. This can be seen in the lower panels of Fig. 8, where much stronger variability in slab rollback is evident for the short SP models, relative to the long SP models (*cf.* Figs 8d and e).

In line with the qualitative mantle flow similarity observed in Fig. 7, the inclusion of a power-law mantle has only a moderate effect on the TPR (Fig. 9). For the short SP model, a power-law mantle rheology reduces $\log_{10}$(TPR) by 0.05–0.1, and for the long SP model, the TPR is approximately equivalent (slightly elevated). As observed in the 2-D models, a power-law mantle rheology decreases trench retreat rate, and so we suggest that the reduction in TPR, for the short SP model, stems from the reduction in relative retreat rate. However, for the long SP model, the relative reduction in trench retreat velocity does not have such an expected effect. We propose that, in addition to the effect that reducing trench retreat has on reducing toroidal flow, the lateral viscosity variations induced by a power-law viscosity promote toroidal flow. As discussed in the next section, a power-law viscosity component has a reduced effect on trench motions for the long SP models (Fig. 10c), and so one may expect the lateral viscosity variation effect to dominate here.

3.2.3 Slab kinematics

As for the 2-D models presented in section 3.1, we find that a power-law mantle rheology reduces the magnitude of trench retreat, V_T, relative to SP velocity, V_P. This is true for each of the SP lengths examined, as shown in Fig. 10 where we plot the temporal evolution of the normalized plate velocities, in the side plate reference frame.

Generally, V_P is greater than V_T (i.e. negative $\log(V_T / V_P)$: Fig. 10c), with the only exception being the isoviscous mantle, long SP model. After the initial, transient bending phase, both plate velocities generally attain a near-constant,

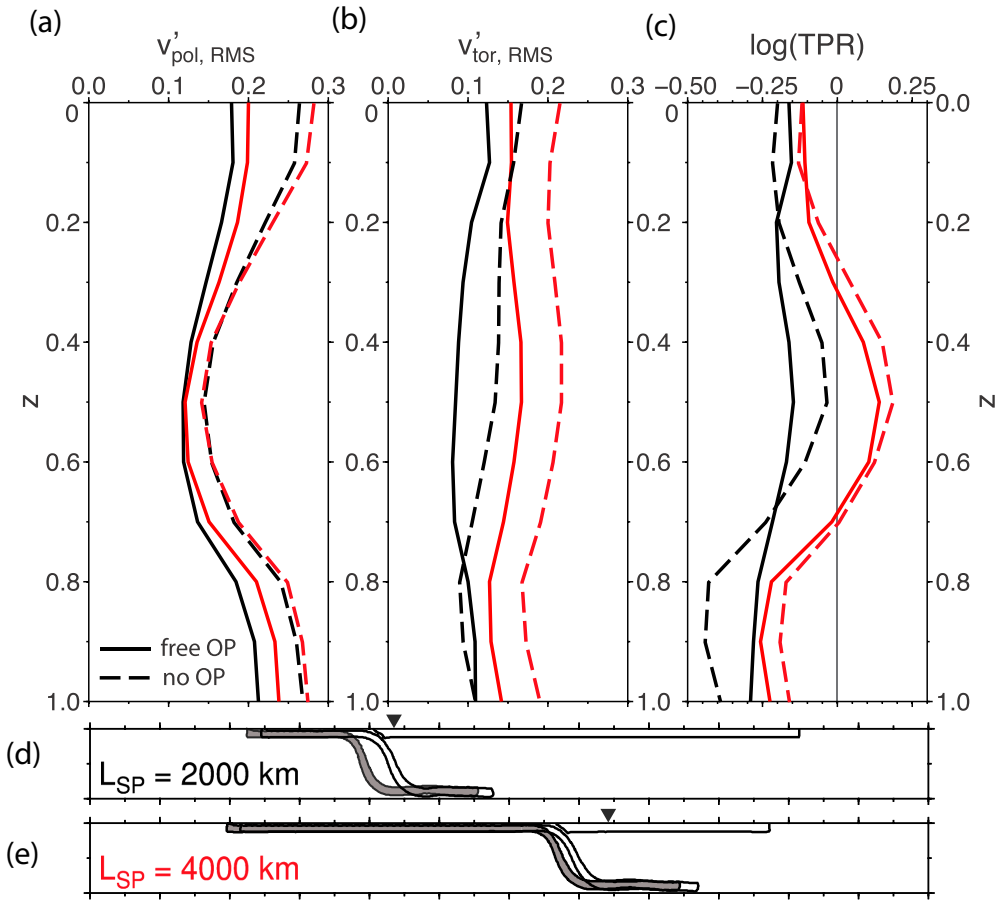

Figure 8. Partitioning of mantle flow between poloidal ($\nabla_h \times \vec{v}_{\rm pol} = 0$) and toroidal ($\nabla_h \cdot \vec{v}_{\rm tor} = 0$) components for models with (solid lines) and without OPs (dashed lines), for the initial SP length end-members (black: $L_{\rm SP} = 2000$ km, red: 4000 km). Shown are vertical profiles, which are composed of velocities averaged over 10 horizontal slices ($\Delta z = 66$ km). Plotted is, (a), RMS of poloidal velocity, (b), RMS of toroidal velocity and, (c), the log ratio of the toroidal to total poloidal RMS velocities. Velocities are normalized by a reference velocity (equivalent for all isoviscous mantle models). Lower panels show corresponding slab morphologies for, (d), $L_{\rm SP} = 2000$ km models with (white slab) and without an OP (grey slab), and, (e), $L_{\rm SP} = 4000$ km models with (white slab) and without an OP (grey slab). Inverted triangles indicate initial trench locations.

steady-state value. As discussed previously, as $L_{\rm SP}$ increases, plate convergence is increasingly accommodated by trench retreat (i.e. V_T / V_P increases). For all plate lengths, the normalized V_P of the power-law rheology models (dashed lines) is generally comparable to the isoviscous mantle models (solid lines). This similarity occurs because the average viscosity used to compute V_{ref} is extracted from SP side of the slab (i.e. the portion of the mantle which dictates V_P). In contrast, the power-law mantle viscosity models exhibit a strong reduction in V_T (Fig. 10b), for all plate geometries. This can be seen in Fig. 10(c), where the temporal evolution of the log of the ratio of V_T and V_P is plotted. For every plate length, $\log(V_T / V_P)$ is consistently reduced in the power-law mantle models. The relative reduction in V_T reduces as the SP length increases (for $L_{\rm SP} = 2000$ km, $\Delta\log(V_T / V_P) \approx 0.15$; for $L_{\rm SP} = 4000$ km, $\Delta\log(V_T / V_P) \approx 0.07$).

We additionally examine isoviscous mantle models with average viscosities equivalent to those observed in the power-law models (as extracted from viscosity profiles taken below the SP). This is done to examine whether the localized viscosity reductions, or the bulk mantle viscosity reduction (which reduces the plate-mantle viscosity contrast), are responsible for the relative V_T reduction. Reducing the mantle viscosity in the Newtonian models does not produce the reduced V_T / V_P observed in the power-law mantle models (Fig. 10c, lighter coloured solid lines). We therefore attribute the reduction in relative trench motions to the localized viscosity reductions that occur directly adjacent to the lithospheric plates in the power-law models.

As in the 2-D models (Fig. 4a), the dip angle increases as power-law deformation becomes more dominant (i.e. as transition strain rate decreases). For the long SP models, Fig. 11 illustrates the dependence of V_T / V_P and the, inversely correlated, slab dip on the transition strain rate. For transition strain rates of 5×10^{-13} s^{-1}, and above, the mantle is almost entirely in the Newtonian regime, and so the slab kinematics are nearly equivalent to those observed in the isoviscous mantle model (Fig. 11). While the sense of kinematic variability is equivalent for the 2-D and 3-D models, the magnitude of variation is not. In 3-D, $\log_{10}(V_T / V_P)$ is reduced by 0.09 for a model with a power-law transition strain rate of 5×10^{-15} s^{-1} (relative to the isoviscous mantle model). The equivalent 2-D models produce a significantly larger reduction of 0.19 (Fig. 4b).

4 DISCUSSION

4.1 Slab dynamics

We employ a simplified parameterization of dislocation creep. However, time-dependent numerical modelling studies that do include

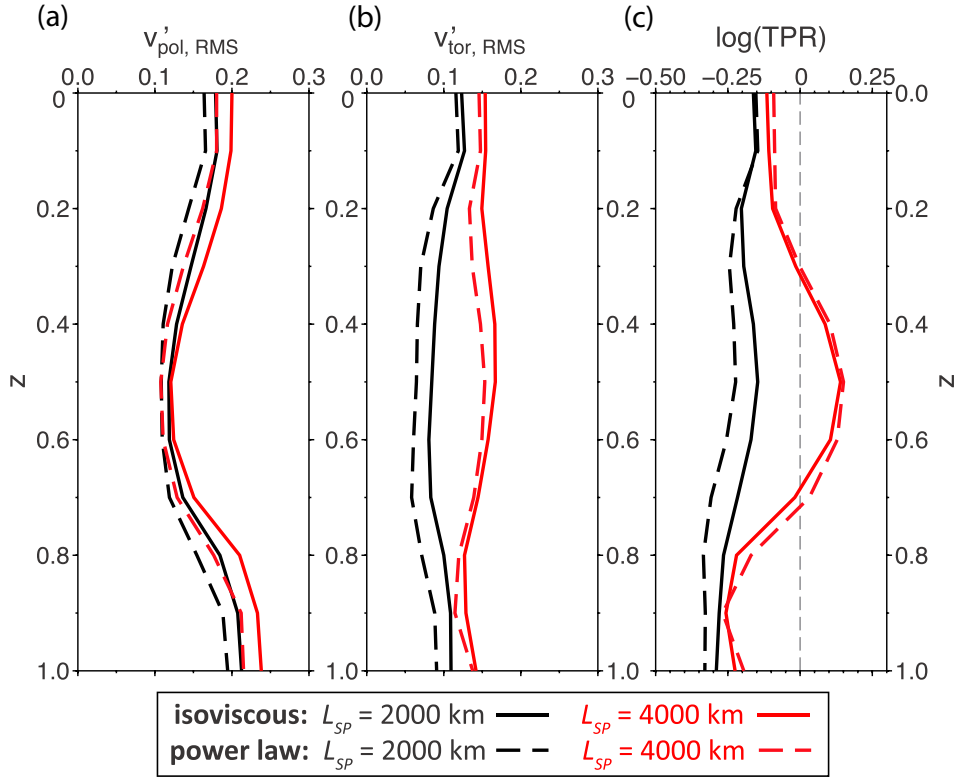

Figure 9. Partitioning of mantle flow between poloidal and toroidal components, for models with an isoviscous mantle (solid lines) and with a power-law rheology with a transition strain rate of 5×10^{-15} s^{-1} (dashed lines). Two initial SP length end-members are plotted (black: $L_{SP} = 2000$ km, red: 4000 km). Shown are vertical profiles, which are composed of velocities averaged over 10 horizontal slices ($\Delta z = 66$ km). Plotted is, (a), RMS of poloidal velocity, (b), RMS of toroidal velocity and, (c), the log ratio of the toroidal to total poloidal RMS velocities. Velocities are extracted at the time steps plotted in Figs 5 and 7, and normalized by a reference velocity as described in the main text.

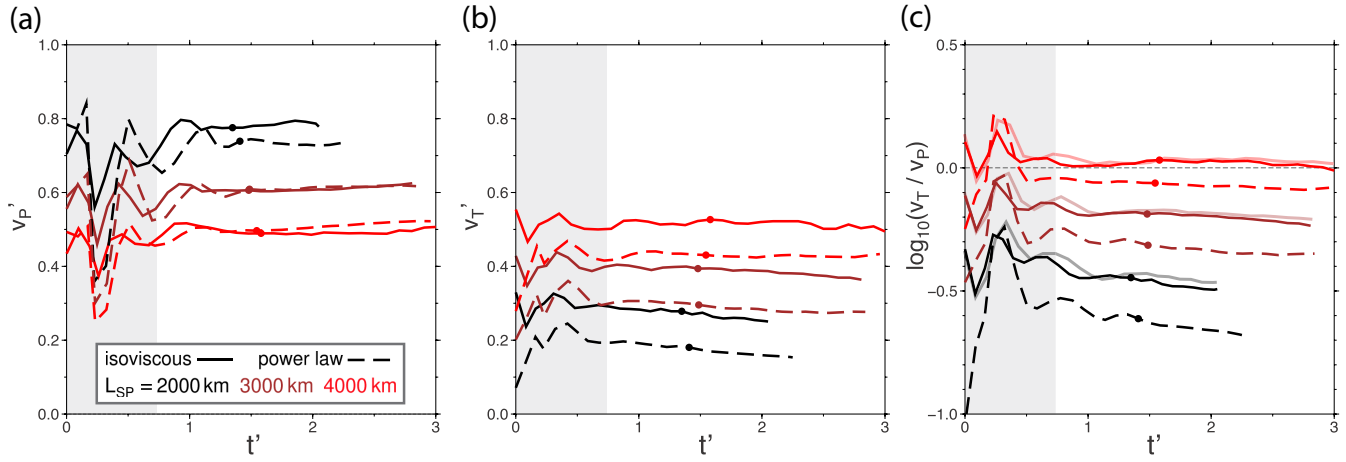

Figure 10. Temporal evolution of plate kinematics for isoviscous mantle (solid lines), and power-law mantle (dashed lines: $\dot{\varepsilon}_{\mathrm{II}}^{T} = 5 \times 10^{-15}$ s^{-1}) models, with variable initial SP lengths. Panels show, (a), the SP velocity (side plate / box reference frame), (b), the trench retreat velocity and, (c), the log of the trench retreat velocity divided by the SP velocity. The lighter, solid lines, on panel (c), display the log ratio for additional Newtonian models which have an average plate–mantle viscosity contrast that is set to be equivalent to that of the power-law models with the same L_{SP}. Plate velocities are normalized by reference velocities computed using sublithospheric viscosities extracted at the time-steps indicated by points. The reference velocity pre-factor is set to give $V_{\mathrm{ref}} = V_C$ for the medium plate length (2000 km), isoviscous mantle model. Grey shading indicates the transient phase, where the slab is bending on top of the lower boundary.

laboratory-derived olivine flow laws tend to observe dislocation creep activation in approximately the same regions as in our models, particularly directly below the lithospheric plates and adjacent to the sinking slab (e.g. Billen & Hirth 2005; Čížková & Bina 2013; Billen & Hirth 2007; Androvičová *et al.* 2013; Garel *et al.* 2014). In addition to broadly matching the depth extent of dislocation creep inferred from seismic anisotropy (see Section 2.1.1), this similarity gives us confidence that our models capture the first order dynamic effects associated with dislocation creep in the upper mantle, provided these models use the 'correct' grain size. As explored in

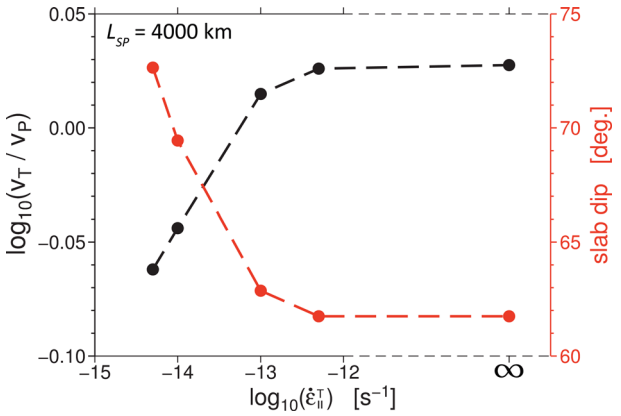

Figure 11. Plate kinematics as a function of transition strain rate, $\dot{\varepsilon}_{II}^{T}$, for the 3-D models with initial $L_{SP} = 4000$ km, extracted at time steps equivalent to those in Figs 5 and 7. Shown is average slab dip angle computed between depths of 200 and 460 km (red), and log ratio of trench retreat velocity and SP velocity (black). The kinematics extracted from the equivalent Newtonian models are placed at an arbitrary, 'infinite' transition strain rate, x-location, for illustrative purposes.

previous work, primary effects of viscosity reductions adjacent to the subducting slab, and in the mantle wedge, include elevated slab sinking/convergence rates, and greater slab dip angles (e.g. Billen & Hirth 2005, 2007; Holt *et al.* 2015a).

As discussed by Billen & Hirth (2005, 2007), this slab dip increase occurs in part due to relative viscosity reductions in the mantle wedge which reduce the magnitude of negative pressure, and so the associated slab-lifting torque (Stevenson & Turner 1977; Tovish *et al.* 1978). This reduction in across-slab dynamic pressure gradient (i.e. $\Delta P_{\text{linear}} - \Delta P_{\text{power-law}}$) is, averaged over the various plate lengths, ∼5 MPa. For an average dip angle of ≈70°, such a reduction in ΔP produces a reduction in the lifting force, $F_{\Delta P}$, of ≈3.5 TN m^{-1} (for our models, $F_{\text{slab pull}} \approx 44$ TN m^{-1}). Billen & Hirth (2005, 2007) hold the trench position fixed and so only consider the role of a reduced ΔP on slab dip angle. However, dip angle is also strongly affected by trench motion, V_T (e.g. Christensen 1996; Ribe 2010). In our numerical models, we find that a power-law mantle viscosity reduces the relative magnitude of trench retreat, which consequently also promotes greater slab dip angles. We, therefore, suggest that allowing the trench to migrate freely will enhance the slab dip increasing effect of dislocation creep. However, a reduction in $F_{\Delta P}$, which has a horizontal component directed towards the mantle wedge, constitutes a reduction in one of the major forces resisting trench retreat (e.g. Royden & Husson 2006; Stegman *et al.* 2006), and so understanding why slabs subducting into a power-law mantle exhibit reduced V_T / V_P requires an analysis of the additional forces associated with mantle flow (Section 4.3).

4.2 Mantle flow and 3-D effects

We have additionally examined the impact of a power-law mantle viscosity on 3-D mantle flow. In our numerical models, we find that a power-law rheology does not significantly impact the mantle flow patterns (*cf.* Christensen 1984), nor the partitioning of flow between poloidal and toroidal components (*cf.* Čadek *et al.* 1993; Becker 2006). When assessing the magnitude of the subduction-resisting forces associated with mantle flow (Section 4.3, Fig. 13), such mantle flow similarity is convenient in that it allows similar expressions to be used to compute mantle shear stresses for both rheologies.

We suggest that the lack of variation in mantle flow partitioning is due to competing power-law effects, namely reduced rollback rates and increased lateral viscosity variations. However, it could also be the case that the transition strain rate imposed in our models, which controls the degree of power-law deformation, is still too high to generate the full extent of dislocation creep active on Earth. Previous numerical modelling studies, which utilize laboratory derived rheologies, report mantle flow velocities that are up to a factor of 8 greater than plate velocities, particularly within the mantle wedge (Billen & Jadamec 2012; Jadamec & Billen 2012). In our study, the relative sublithospheric mantle flow velocities (i.e. normalized by the plate velocity) are typically only 5–10 per cent greater for the reference power-law, composite rheology model (Figs 12a and c). However, a direct comparison is complicated by the complex subduction geometry, and strong lithospheric plates (on average, four orders of magnitude stronger than the asthenosphere) considered in the studies mentioned above. Also, these studies compute instantaneous flow and so it is not obvious that stable subduction would occur for time-dependent versions of these setups. A combination of these two modelling strategies, that is, dynamically evolving 3-D subduction and a laboratory-derived rheological parameterization, is therefore required to further assess the impact of dislocation creep on subduction-induced mantle flow.

In all of the models explored, there are multiple regions with significant upwards-directed, vertical mantle flow. In addition to upwelling flow at the trailing edges of the two plates, a vigorous mantle upwelling occurs at the lateral edge of the slab-tip, and more moderate vertical flow is associated with flow around the slab edge (i.e. subhorizontal toroidal flow cell). These flow features are consistent with the study of Faccenna *et al.* (2010), where these types of upwellings are observed in single slab numerical models, and invoked to explain the anomalous off-arc volcanism observed in locations such as the western US and the Mediterranean, and the analogue modelling studies of Schellart (2010) and Strak & Schellart (2014). Our models verify the presence of such upwellings in dynamic subduction models that incorporate both an OP, and a stress-dependent mantle rheology. Additionally, beneath the OP and ∼500 km away from the trench, we observe moderate power-law deformation which could have potential implications for melt/volatile transportation in the mantle wedge/forearc region.

Relative to the 2-D models, we find that the magnitude of variation of both slab dip and trench retreat rates induced by variable mantle rheology is significantly reduced in 3-D. In 3-D, the presence of a finite width trench enables toroidal mantle flow around the slab edge, which can act to relieve subslab pressures, thereby enabling rapid trench retreat (e.g. Funiciello *et al.* 2003; Schellart 2004; Royden & Husson 2006; Stegman *et al.* 2006, 2010). However, in 2-D, such a mechanism for relieving elevated subduction pressures is absent. Therefore, the variation in across-slab pressure gradient induced by mantle rheology is likely to be greater in 2-D, and thus require greater variation in the slab kinematics to accommodate this (i.e. satisfy the appropriate force balances). The presence of a viscous lower mantle, neglected here for simplicity, may reduce the magnitude of this 2-D effect by enabling subslab pressure build-up to be relieved by deep, poloidal flow (e.g. Husson *et al.* 2012).

4.3 A mechanism for reduced trench retreat

A simplified analysis of the magnitudes of the forces resisting subduction may provide further insights into why a power-law asthenospheric viscosity component promotes subduction to occur

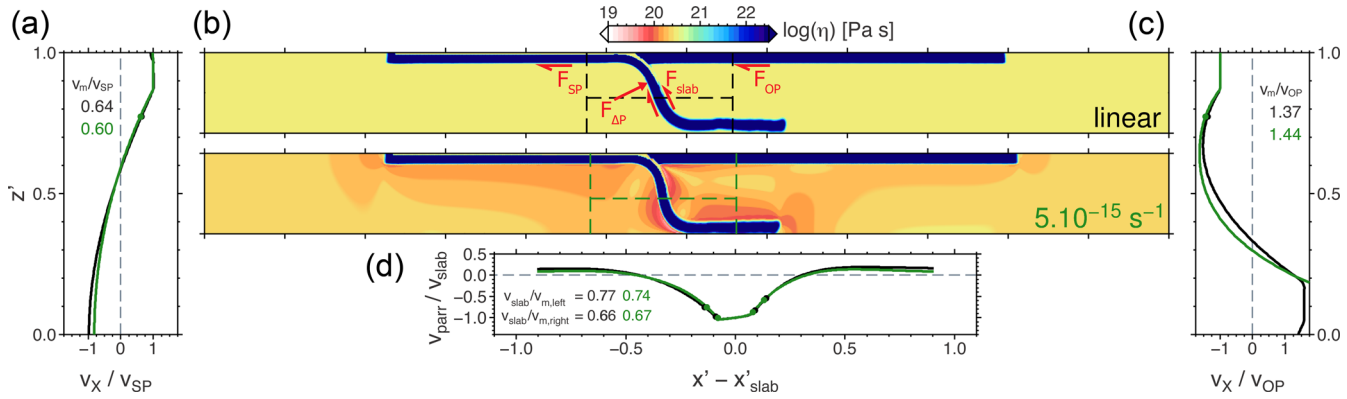

Figure 12. Mantle flow profiles for the medium SP models ($L_{SP} = 3000$ km), with both an isoviscous mantle and a transition strain rate of 5×10^{-15} s^{-1}. Shown are vertical profiles of (normalized) horizontal velocity (v_X) extracted, (a), 600 km from the left of the slab (i.e. sub-SP mantle), and, (c) 600 km to the right of the slab (i.e. sub-OP mantle). Also shown are, (b), model viscosity fields and, d), slab parallel mantle velocity (v_{parr}) extracted along a horizontal profile at mid-mantle depth ($z = 370$ km), normalized by the slab sinking velocity (v_{slab}). Panel (a) includes red arrows illustrating the direction of the mantle forces used in the subsequent force comparison (Fig. 13). Indicated by text (panels a, c and d) are mantle over plate/slab velocity ratios ($\Delta z = 70$ km, $\Delta x = 50$ km).

preferentially via SP motion, V_P, as opposed to trench retreat, V_T. Previous studies have utilized adaptations of the expression derived by Conrad & Hager (1999), which consists of a balance between slab pull and the subduction-resisting forces (i.e. slab bending, mantle drag, and interfacial coupling), to predict convergence rates (V_C) for a range of lithospheric properties (e.g. Funiciello *et al.* 2003; Bellahsen *et al.* 2005). Here, we instead compute approximations of the forces resisting both trench retreat and SP motion, for our observed V_C and across-slab pressure gradients (ΔP). We focus on the forces associated with mantle flow, as these are the force components directly modified by the presence of a power-law rheology. Therefore, we do not explicitly consider slab pull and slab bending which, respectively, drive and resist subduction, in an approach similar to that of Schmeling *et al.* (2005).

While the inclusion of a power-law viscosity component significantly modifies the mantle viscosity (e.g. Fig. 5), the style of subduction-induced mantle return flow is comparable for models with and without such a mantle rheology (Fig. 7). We therefore assume that the ratios between the plate/slab velocities and the adjacent mantle velocities are equivalent for both mantle rheologies. We compute the plate/mantle velocity ratios from the intermediate SP length model ($L_{SP} = 3000$ km), and then simply use the value averaged over both rheologies for the subsequent shear force calculations. Fig. 12 shows the mantle velocity profiles used for this calculation and verifies the similarity between the flow profiles for the two models. Beneath the SP, the asthenosphere is flowing slower than the plate, and so exerts basal tractions which resist SP motion, V_P (Fig. 12a). Conversely, the subduction-induced flow beneath the OP is faster than the plate motion which results in basal tractions that are driving trench-wards OP motion (Fig. 12c). The subduction-resisting shear force per unit length on the SP is given by the product of an average sublithospheric shear stress and the SP length,

$$F_{SP} = (2\eta_{m,SP}\dot{\varepsilon}_{shear})X_{SP} \approx \eta_{m,SP}\left(\frac{V_P - V_{m,P}}{\Delta z}\right)X_{SP}, \tag{4}$$

where V_P and $V_{m,P}$ are, respectively, the SP velocity and the horizontal velocity of sublithospheric mantle, and Δz is the depth that $V_{m,P}$ is extracted at, relative to the base of the lithospheric plate (e.g. Fig. 12a). This assumes that the horizontal gradient of vertical velocity is negligible, as can be seen from the mantle flow field (e.g., Fig. 5). $\eta_{m,SP}$ is the average sublithospheric viscosity beneath the SP, and X_{SP} is the SP length over which this average shear stress acts ($\approx L_{SP} - 1000$ km). Similarly, the OP motion-driving force is given by,

$$F_{OP} \approx \eta_{m,OP}\left(\frac{V_C - V_P - V_{m,OP}}{\Delta z}\right)X_{OP}, \tag{5}$$

where V_C is the convergence rate ($= V_T + V_P$), and X_{OP} is the approximate OP length over which this average shear stress acts. X_{OP} does not appear to have a dependence on plate length and so, based on inspection of Fig. 12 and similar figures with flow profiles plotted at different distances from the slab, we use an average X_{OP} of 1200 km. In addition we compute the approximate, up-dip directed shear force, F_{slab}, acting on the slab,

$$F_{slab} \approx 2\eta_{m,slab}\left(\frac{V_C - V_{m,slab}}{\Delta n}\right)\frac{h}{\sin(\theta)}, \tag{6}$$

where $V_{m,slab}$ is the slab-parallel mantle flow velocity at a slab-normal distance of Δn away from the slab edge, h is the depth-extent of the slab ($= 660$ km$-h_l = 580$ km), and θ is the dip angle. The additional factor 2 occurs due to mantle shear occurring on both sides of the slab. In the power-law numerical models, mantle viscosity is a function of the deviatoric strain rate, $\dot{\varepsilon}_{II}$ (i.e. eq. 2). Under the assumption that the only non-zero strain rate component is the shear strain rate (in the vertical plane), $\dot{\varepsilon}_{II} = \dot{\varepsilon}_{shear}$, and so, for example, the power-law component of the sublithospheric viscosity below the SP can be written as

$$\eta^P_{SP} = \eta^N\left(\frac{V_P - V_{m,P}}{2\,\Delta z\,\dot{\varepsilon}^T_{II}}\right)^{\frac{1-n}{n}}, \tag{7}$$

which is then combined with η^N_{mantle} to get the effective, sublithospheric viscosity (eq. 1), and inserted into the expression for F_{SP} (eq. 4). An approximation for the total, mantle force resisting SP motion, V_P, is taken to be the sum of the subduction-resisting shear forces associated with the flat-lying portion of the SP and the slab, $F_P = F_{SP} + F_{slab}$. Similarly, the approximate, mantle-derived, force resisting trench retreat is composed of a component associated with an along-slab mantle pressure gradient, ΔP, and the force driving OP motion, i.e. $F_T = F_{\Delta P} - F_{OP}$. The directions of each of these forces considered are shown on Fig. 12(a). Within this F_T is the assumption that F_{OP}—the horizontal mantle shear force on the OP—is transmitted to the SP in the form of a horizontal force promoting rollback (i.e. by 'pushing' the slab hinge, e.g. van

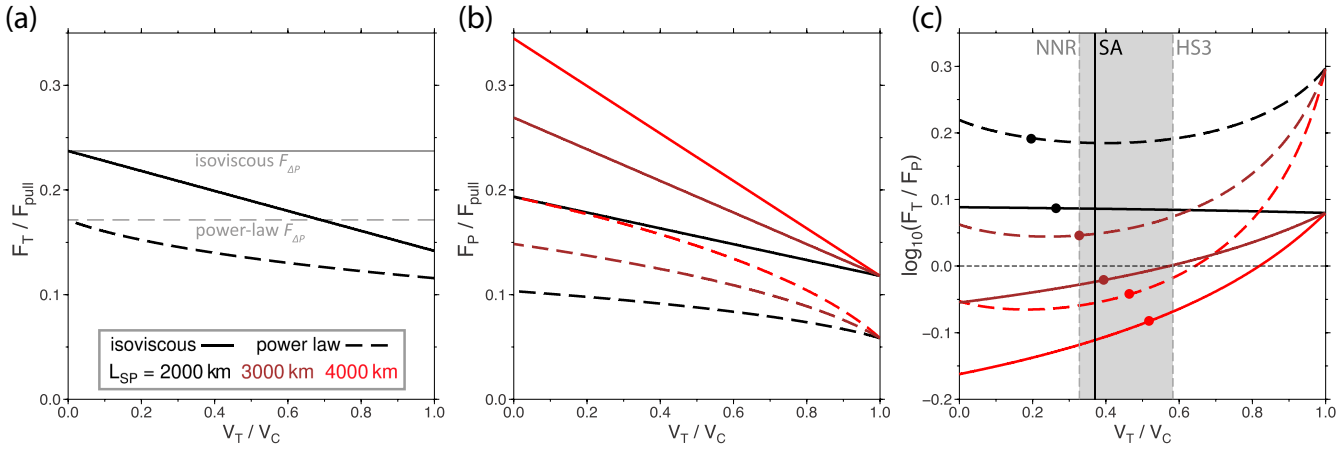

Figure 13. Simplified analytical calculations of the trench retreat, and SP motion, resisting forces for isoviscous and power-law mantle rheologies ($\dot{\varepsilon}_{II}^{T} = 5 \times 10^{-15}$ s^{-1}). Plotted is, (a), the force resisting trench retreat, (b), the force resisting SP motion, and, (c), the log ratio of the two forces. All forces are plotted as a function of the trench retreat velocity (V_T) over the total convergence rate (V_C), and normalized by the slab pull force (= 44 TN m^{-1}). Curves corresponding to each of the subducting plate lengths are shown (in our approximation, F_T is not a function of L_{SP}). The filled circles indicate the V_T / V_C observed in the numerical models for the corresponding rheology and L_{SP}. Also included on panel c) are vertical bars indicating the median V_T / V_C in three different reference frames: No-net rotation (0.33), spreading-aligned (0.37), and hotspot (0.58) (Gripp & Gordon 2002; Kreemer *et al.* 2003; Becker *et al.* 2015). Average kinematic properties used for the calculation (extracted from the numerical models) are listed in the main text.

Dinther *et al.* 2010). While a proportion of F_{OP} is likely dissipated in the weak plate boundary, we neglect this in order to simplify our calculations. The other component of the force resisting trench retreat, the horizontal component of $F_{\Delta P}$, is computed using the average pressure gradient extracted from our numerical models ($F_{\Delta P} = \Delta P(h / \sin(\theta))$. ΔP is computed using two points 330 km either side of the slab, at mid-mantle depths ($z = 330$ km).

We consider a power-law rheology equivalent to that implemented in the numerical models, with a transition strain rate of 5×10^{-15} s^{-1}. As input into our simplified model we use the average θ, V_C, and ΔP observed in the isoviscous (65°, 6.9 cm yr^{-1}, 18 MPa) and power-law mantle viscosity models (75°, 10.3 cm yr^{-1}, 13 MPa), but ignore variation associated with the variable plate lengths in order to keep the calculations general. We do however include the average variability because the power-law reduction in ΔP and increase in V_C both promote trench retreat (in our calculation), and so we wanted to determine whether, despite this, the relative force resisting trench motion would increase.

Fig. 13 shows the magnitude of the calculated trench resisting (F_T) and plate motion resisting forces (F_P), normalized by the slab pull force (= 44 TN m^{-1}), as a function of relative trench motion, V_T / V_C (i.e. 0 = pure plate motion, 1 = pure trench motion). For a fixed trench, F_T is composed solely of the resisting force associated with mantle pressure (Fig. 13a). With increasing trench motion, the trench retreat resisting force reduces, as a result of an increasing F_{OP} which acts to promote retreat (eq. 5). The magnitude of this reduction in F_T is lower when a power-law rheology is considered, as F_{OP} reduces due to the relative reduction in asthenospheric viscosity. The force resisting plate motion, F_P, is shown in Fig. 13(b). Generally, F_P is reduced for the power-law models. This occurs because the magnitude of the subduction-resisting shear tractions associated with both the flat-lying portion of the SP (F_{SP}), and the slab (F_{slab}), are reduced when a power-law viscosity is considered. Additionally, models with longer SPs have elevated F_P due to the effect of increasing X_{SP} on F_{SP}, and the curves have negative trends due to the dependence of F_{SP} on V_P (eq. 4).

We plot the ratio of the trench retreat resisting force and the plate motion resisting force, F_T / F_P (Fig. 13c). Also included on Fig. 13(c) are points indicating the V_T / V_C values observed in our numerical models, and the present day, median V_T / V_C values observed on Earth (Heuret & Lallemand 2005), for a range of APM reference frames. As the trenches in our numerical models are, by design, retreating, we consider only retreating trenches for the plotted Earth V_T / V_C averages. However, we note that the V_T / V_C range is comparable when advancing trenches are included (i.e. with advancing trenches: $V_T / V_C = 0.32-0.55$; without advancing trenches: 0.33−0.58). Our models generally lie within these kinematic ranges, with the exception of the short SP models ($L_{SP} = 2000$ km), in which V_P is overly dominant (Fig. 13c).

We consider F_T / F_P to be an approximate measure of the degree to which the mantle forces favour trench retreat (i.e. low values) or plate motion. This measure does not consider other important forces, both driving (i.e. slab pull) and resisting (e.g. slab bending), in the system, and so only constitutes an approximate metric for plate versus trench motion. However, it does mirror the first-order features observed in the slab kinematics (Fig. 10c), suggesting that mantle-related forces exert an important control on slab kinematics (*cf.* Schmeling *et al.* 2005). Firstly, plate motion is increasingly favoured as L_{SP} decreases, as observed in the numerical models. This occurs primarily because the plate motion resisting force, F_{SP}, reduces as L_{SP} decreases. More importantly, F_T / F_P is elevated for the power-law models for all plate lengths. This consistent increase in the relative F_T is a robust feature of the analysis, regardless of whether we include individual model values for ΔP and θ (i.e. no averaging), or use the same values for all models (i.e. increased averaging). This occurs because the localized viscosity reductions induced by the power-law rheology reduce the mantle shear resistance to both horizontal plate sliding (F_{SP}) and slab sinking (F_{slab}), to a greater degree than a reduction in mantle wedge pressure ($F_{\Delta P}$) reduces the mantle resistance to trench retreat. We therefore suggest that it is these effects which preferentially promote SP motion, over trench retreat, for the models with a power-law mantle viscosity component.

Our numerical models with reduced, bulk mantle viscosities do not produce such a reduction in relative trench retreat rate (Fig. 10c), and so we emphasize that this is an effect of relative viscosity

reductions adjacent to the lithospheric plates. This constitutes an example of reduced sublithospheric shear stresses shifting the partitioning of plate convergence between plate and trench motion. While we focus here on power-law deformation, such localized viscosity reductions could potentially also occur due to volatile enrichment and/or mantle melting.

4.4 Model and analysis limitations

While this force analysis has enabled us to probe the mantle forces that control the partitioning of subduction between rollback and plate advance for our observed kinematics, it does not allow us to directly predict V_T / V_P. Full force balances, which include the additional important forces (i.e. slab pull, slab bending, plate interface coupling) (e.g. Royden & Husson 2006; Billen 2008), are required to dynamically compute V_C and ΔP, and so in turn assess the magnitude of this effect for various subduction setups (e.g., lithospheric and mantle strengths). However, simply extracting these components from the numerical models is sufficient to illustrate our proposed mechanism for trench retreat reduction.

Our force assessment focuses on the variation in mantle forcing as a function of mantle rheology, thereby neglecting forces directly associated with the lithospheric plates. This is reasonable as slab density, viscosity, and thickness are fixed throughout this study. An exception, and potential source of lithospheric-induced force variation, is the variation of slab radius of curvature, R, which exerts a strong control on the slab bending force for a viscous slab $F_B \propto \eta_l v_C (h_l / R)^3$ (Conrad & Hager 1999), as a function of both mantle rheology and time (e.g. Becker *et al.* 1999; Buffett 2006; Stegman *et al.* 2006; Capitanio *et al.* 2009). Further work is therefore required to assess potential feedbacks between slab curvature and a stress dependent mantle rheology, in order to untangle this component of the slab force balance and determine its expected kinematic expression.

While a simplified setup has allowed us to extract the first order effects of a power-law mantle rheology on slab kinematics, we suggest that both the lithospheric rheology and the properties of the lower mantle may play important roles. The rate of trench retreat and the degree of subducting slab weakening, in the form of plastic yielding or a maximum viscosity cut-off, have been demonstrated to exert first order controls on the propensity of a slab to penetrate into a strong lower mantle (e.g. Zhong & Gurnis 1995; Christensen 1996; Čížková *et al.* 2002; Enns *et al.* 2005; Billen 2008). Future work focused on understanding how slab impingement upon a strong lower mantle influences the rollback systematics observed here is required to refine our understanding of trench retreat rate reduction due to power-law mantle deformation.

5 CONCLUSIONS

We used 3-D, dynamic models of subduction to address the role of a power-law mantle viscosity on rates of trench retreat. For a suite of models that exhibit a broad range of slab kinematics, we find that a power-law rheology results in reduced rates of trench retreat, V_T and elevated slab dip angles, relative to the equivalent isoviscous mantle models. We analyse the style of mantle flow, which exhibits only limited variability as a function of mantle rheology, and mantle pressure, in order to compute estimates of the forces resisting both V_T, and SP advance, V_P. We find that the inclusion of a power-law rheology reduces the mantle shear force, which resists V_P, to a greater extent than it reduces the dynamic pressure gradient across the slab, which resists V_T. Thus, the inclusion of a power-law mantle rheology favours a shift towards a subduction mode with a reduced trench retreat component. In addition to the inclusion of an OP, we suggest that this mechanism may be of key importance in reducing the high relative V_T rates often observed in single slab models to levels more in line with the average subduction partitioning observed on Earth (i.e. $V_T \leq V_P$). More sophisticated numerical models, and analytical force balances, are required to more rigorously map out the 'Earth-like' parameter space where this mechanism is viable.

ACKNOWLEDGEMENTS

This manuscript benefitted from the comments of editor Juan Afonso, reviewer Dave Stegman, and one anonymous. We would also like to thank Wiki Royden for her contributions to developing the reference model, and discussions which substantially improved this work. We thank the original authors and CIG (geodynamics.org) for providing CitcomCU. Computations were performed on USC's High Performance Computing Center, and most figures were made with the Generic Mapping Tools (Wessel *et al.* 2013).

REFERENCES

Androvičová, A., Čížková, H. & van den Berg, A.P., 2013. The effects of rheological decoupling on slab deformation in the Earth's upper mantle, *Stud. Geophys. Geod.,* **57,** 460–481.

Becker, T.W., 2006. On the effect of temperature and strain-rate dependent viscosity on global mantle flow, net rotation, and plate-driving forces, *Geophys. J. Int.,* **167,** 943–957.

Becker, T.W. & Faccenna, C., 2009. A review of the role of subduction dynamics for regional and global plate motions, in *Subduction Zone Geodynamics,* pp. 3–34, eds Lallemand, S. & Funiciello, F., Springer.

Becker, T.W., Faccenna, C., O'Connell, R.J. & Giardini, D., 1999. The development of slabs in the upper mantle: insights from experimental and laboratory experiments, *J. geophys. Res.,* **104,** 15 207–15 226.

Becker, T.W., Schaeffer, A.J., Lebedev, S. & Conrad, C.P., 2015. Toward a generalized plate motion reference frame, *Geophys. Res. Lett.,* **42,** 3188–3196.

Behn, M.D., Hirth, G. & Elsenbeck, J.R., 2009. Implications of grain size evolution on the seismic structure of the oceanic upper mantle, *Earth planet. Sci. Lett.,* **282,** 178–189.

Běhounková, M. & Čížková, H., 2008. Long-wavelength character of subducted slabs in the lower mantle, *Earth planet. Sci. Lett.,* **275,** 43–53.

Bellahsen, N., Faccenna, C. & Funiciello, F., 2005. Dynamics of subduction and plate motion in laboratory experiments: Insights into the "plate tectonics" behavior of the Earth, *J. geophys. Res.,* **110,** doi:10.1029/2004JB002999.

Bercovici, D., 1993. A simple model of plate generation from mantle flow, *Geophys. J. Int.,* **114,** 635–650.

Billen, M.I., 2008. Modeling the dynamics of subducting slabs, *Annu. Rev. Earth Planet. Sci.,* **36,** 325–356.

Billen, M.I. & Gurnis, M., 2005. Constraints on subducting plate strength within the Kermadec trench, *J. geophys. Res.,* **110,** doi:10.1029/2004JB003308.

Billen, M.I. & Hirth, G., 2005. Newtonian versus non-Newtonian upper mantle viscosity: implications for subduction initiation, *Geophys. Res. Lett.,* **32,** L19304, doi:10.1029/2005GL023457.

Billen, M.I. & Hirth, G., 2007. Rheologic controls on slab dynamics, *Geochem. Geophys. Geosyst.,* **8,** Q08012, doi:10.1029/2007GC001597.

Billen, M.I. & Jadamec, M., 2012. Origin of localized fast mantle flow velocity in numerical models of subduction, *Geochem. Geophys. Geosyst.,* **13,** doi:10.1029/2011GC003856.

Buffett, B.A., 2006. Plate force due to bending at subduction zones, *J. geophys. Res.,* **111,** doi:10.1029/2006JB004295.

Butterworth, N.P., Quevedo, L., Morra, G. & Müller, R.D., 2012. Influence of overriding plate geometry and rheology on subduction, *Geochem. Geophys. Geosyst.,* **13,** doi:10.1029/2011GC003968.

Buttles, J. & Olson, P., 1998. A laboratory model of subduction zone anisotropy, *Earth planet. Sci. Lett.,* **164,** 245–262.

Byerlee, J.D., 1968. Brittle-ductile transition in rocks, *J. geophys. Res.,* **73,** 4741–4750.

Čadek, O., Ricard, Y., Martinec, Z. & Matyska, C., 1993. Comparison between Newtonian and non-Newtonian flow driven by internal loads, *Geophys. J. Int.,* **112,** 103–104.

Capitanio, F.A., Morra, G. & Goes, S., 2009. Dynamics of plate bending at the trench and slab-plate coupling, *Geochem. Geophys. Geosyst.,* **10,** doi:10.1029/2008GC002348.

Capitanio, F.A., Stegman, D.R., Moresi, L. & Sharples, W., 2010. Upper plate controls on deep subduction, trench migrations and deformations at convergent margins, *Tectonophysics,* **483,** 80–92.

Carlson, R.L. & Melia, P.J., 1984. Subduction hinge migration, *Tectonophysics,* **102,** 1–16.

Christensen, U., 1984. Convection with pressure- and temperature-dependent non-Newtonian rheology, *Geophys. J. R. astr. Soc.,* **77,** 343–384.

Christensen, U., 1996. The influence of trench migration on slab penetration into the lower mantle, *Earth planet. Sci. Lett.,* **140,** 27–39.

Čížková, H. & Bina, C., 2013. Effects of mantle and subduction-interface rheologies on slab stagnation and trench rollback, *Earth planet. Sci. Lett.,* **379,** 95–103.

Čížková, H., van Hunen, J., van den Berg, A.P. & Vlaar, N.J., 2002. The influence of rheological weakening and yield stress on the interaction of slabs with the 670-km discontinuity, *Earth planet. Sci. Lett.,* **199,** 447–457.

Conrad, C. & Hager, B., 1999. Effects of plate bending and fault strength at subduction zones on plate dynamics, *J. geophys. Res.,* **104,** 17 551–17 571.

Di Giuseppe, E., van Hunen, J., Funiciello, F., Faccenna, C. & Giardini, D., 2008. Slab stiffness control of trench motion: Insights from numerical models, *Geochem. Geophys. Geosyst.,* **9,** doi:10.1029/2007GC001776.

Duarte, J.C., Schellart, W.P. & Cruden, A.R., 2013. Three-dimensional dynamic laboratory models of subduction with an overriding plate and variable interplate rheology, *Geophys. J. Int.,* **195,** 47–66.

Dvorkin, J., Nur, A., Mavko, G. & Ben-Avraham, Z., 1993. Narrow subducting slabs and the origin of backarc basins, *Tectonophysics,* **227,** 63–79.

Elsasser, W.M., 1971. Sea-floor spreading as thermal convection, *J. geophys. Res.,* **76**(5), 1101–1112.

Enns, A., Becker, T.W. & Schmeling, H., 2005. The dynamics of subduction and trench migration for viscosity stratification, *Geophys. J. Int.,* **160,** 761–775.

Faccenna, C., Di Giuseppe, E., Funiciello, F., Lallemand, S. & van Hunen, J., 2009. Control of sea floor aging on the migration of the Izu-Bonin-Mariana trench, *Earth planet. Sci. Lett.,* **288,** 386–398.

Faccenna, C., Becker, T.W., Lallemand, S., Lagabrielle, Y., Funiciello, F. & Piromallo, C., 2010. Subduction-triggered magmatic pulses. a new class of plumes?, *Earth planet. Sci. Lett.,* **209,** 54–68.

Forsyth, D. & Uyeda, S., 1975. On the relative importance of the driving forces of plate motion, *Geophys. J. R. astr. Soc.,* **43,** 163–200.

Funiciello, F., Morra, G., Regenauer-Lieb, K. & Giardini, D., 2003. Dynamics of retreating slabs: 1. Insights from two-dimensional numerical experiments, *J. geophys. Res.,* **108,** doi:10.1029/2001JB000898.

Funiciello, F., Faccenna, C. & Giardini, D., 2004. Flow in the evolution of subduction system: Insights from 3-D laboratory experiments, *Geophys. J. Int.,* **157,** 1393–1407.

Funiciello, F., Faccenna, C., Heuret, A., Lallemand, S., Di Giuseppe, E. & Becker, T.W., 2008. Trench migration, net rotation and slab-mantle coupling, *Earth planet. Sci. Lett.,* **271,** 233–240.

Garel, F., Goes, S., Davies, D.R., Davies, J.H., Kramer, S.C. & Wilson, C.R., 2014. Interaction of subducted slabs with the mantle transition-zone: a regime diagram from 2-D thermo-mechanical models with a mobile trench and an overriding plate, *Geochem. Geophys. Geosyst.,* **15,** doi:10.1002/2014GC005257.

Gripp, A.E. & Gordon, R., 2002. Young tracks of hotspots and current plate velocities, *Geophys. J. Int.,* **150,** 321–361.

Heuret, A. & Lallemand, S., 2005. Plate motions, slab dynamics and back-arc deformation, *Phys. Earth planet. Inter.,* **149,** 31–51.

Hirth, G. & Kohlstedt, D.L., 2003. Rheology of the upper mantle and the mantle wedge: a view from the experimentalists, in *Inside the Subduction Factory,* vol. 138, pp. 83–105, ed. Eiler, J., American Geophysical Union.

Holt, A., Becker, T.W. & Buffett, B.A., 2015a. Trench migration and overriding plate stress in dynamic subduction models, *Geophys. J. Int.,* **201,** 172–192.

Holt, A., Buffett, B.A. & Becker, T.W., 2015b. Overriding plate thickness control on subducting plate curvature, *Geophys. Res. Lett.,* **42,** 3802–3810.

Honda, S., 2009. Numerical simulations of mantle flow around slab edges, *Earth planet. Sci. Lett.,* **277,** 112–122.

Husson, L., Conrad, C.P. & Faccenna, C., 2012. Plate motions, Andean orogeny, and volcanism above the South Atlantic convection cell, *Earth planet. Sci. Lett.,* **317,** 126–135.

Jacoby, W.R., 1973. Model experiment of plate movements, *Nature,* **242,** 130–134.

Jadamec, M.A. & Billen, M.I., 2012. The role of rheology and slab shape on rapid mantle flow: 3D numerical models of the Alaska slab edge, *J. geophys. Res.,* **117,** B02304, doi:10.1029/2011JB008563.

Jagoutz, O., Royden, L., Holt, A.F. & Becker, T.W., 2015. Anomalously fast convergencve of india and eurasia caused by double subduction, *Nat. Geosci.,* **8,** 475–478.

Jarrard, R.D., 1986. Relations among subduction parameters, *Rev. Geophys.,* **24,** 217–284.

Karato, S. & Wu, P., 1993. Rheology of the upper mantle: a synthesis, *Science,* **260,** 771–778.

Kincaid, C. & Griffiths, R.W., 2003. Laboratory models of the thermal evolution of the mantle during rollback subduction, *Nature,* **245,** 58–62.

King, S., 2016. Reconciling laboratory and observational models of mantle rheology in geodynamic modelling, *J. Geodyn.,* **100,** 33–50.

Kreemer, C., Holt, W.E. & Haines, A.J., 2003. An integrated global model of present-day plate motions and plate boudnary deformation, *Geophys. J. Int.,* **154,** 5–34.

Lallemand, S. & Heuret, A., 2005. On the relationships between slab dip, back-arc stress, upper plate absolute motion, and crustal nature in subduction zones, *Geochem. Geophys. Geosyst.,* **6,** doi:10.1029/2005GC000917.

Lallemand, S., Heuret, A., Faccenna, C. & Funiciello, F., 2008. Subduction dynamics as revealed by trench migration, *Tectonics,* **27**(TC3014), doi:10.1029/2007TC002212.

Long, M.D. & Becker, T.W., 2010. Mantle dynamics and seismic anisotropy, *Earth planet. Sci. Lett.,* **297**(3), 341–354.

McNamara, A.K. & Zhong, S., 2004. Thermochemical structures within a spherical mantle: superplumes or piles?, *J. geophys. Res.,* **109,** doi:10.1029/2003JB002847.

Moresi, L.N. & Gurnis, M., 1996. Constraints on the lateral strength of slabs from three-dimensional dynamic flow models, *Earth planet. Sci. Lett.,* **138,** 15–28.

Nicolas, A. & Christensen, N.I., 1987. Formation of anisotropy in upper mantle peridotites; a review, in *Composition, structure and dynamics of the lithosphere-asthenosphere system,* Vol. 16, pp. 111–123, eds Fuchs, K. & Froidevaux, C., American Geophysical Union.

Petersen, R.I., Stegman, D.R. & Tackley, P.J., 2015. A regime diagram of mobile lid convection with plate-like behavior, *Phys. Earth planet. Inter.,* **241,** 65–76.

Piromallo, C., Becker, T.W., Funiciello, F. & Faccenna, C., 2006. Three-dimensional instantaneous mantle flow induced by subduction, *Geophys. Res. Lett.,* **33,** L08304, doi:10.1029/2005GL025390.

Podolefsky, N.S., Zhong, S. & McNamara, A.K., 2004. The anisotropic and rheological structure of the oceanic upper mantle from a simple model of plate shear, *Geophys. J. Int.,* **158,** 287–296.

Ribe, N.M., 2010. Bending mechanics and mode selection in free subduction: a thin-sheet analysis, *Geophys. J. Int.,* **180,** 559–576.

Royden, L.H. & Husson, L., 2006. Trench motion, slab geometry and viscous stresses in subduction systems, *Geophys. J. Int.,* **167,** 881–895.

Schellart, W.P., 2004. Kinematics of subduction and subduction-induced flow in the upper mantle, *J. geophys. Res.,* **109**(B7), doi:10.1029/2004JB002970.

Schellart, W.P., 2010. Mount Etna-Iblean volcanism caused by rollback-induced upper mantle upwelling around the ionian slab edge: an alternative to the plume model, *Geology,* **38**(8), 691–694.

Schellart, W.P. & Moresi, L., 2013. A new driving mechanism for backarc extension and backarc shortening through slab sinking induced toroidal and poloidal mantle flow: Results from dynamic subduction models with an overriding plate, *J. geophys. Res.,* **118,** 3221–3248.

Schellart, W.P., Freeman, J., Stegman, D.R., Moresi, L. & May, D.A., 2007. Evolution and diversity of subduction zones controlled by slab width, *Nature,* **446,** 308–311.

Schellart, W.P., Stegman, D.R. & Freeman, J., 2008. Global trench migration velocities and slab migration induced upper mantle volume fluxes: Constraints to find an Earth reference frame based on minimizing viscous dissipation, *Earth Sci. Rev.,* **88,** 118–144.

Schmeling, H., Enns, A. & Ullmann, S., 2005. What is the cause for trench rollback?, in *9th International Workshop on Numerical Modeling of Mantle Convection and Lithospheric Dynamics, Abstracts,* Ettore Majorana Foundation and Centre for Scientific Culture, Erice, Italy, available at http://www.earthsinterior.de/Workshop.2005/PDF/Erice_Abstracts.pdf, accessed August 2016.

Schott, B. & Schmeling, H., 1998. Delamination and detachment of a lithospheric root, *Tectonophysics,* **296,** 225–247.

Sharples, W., Jadamec, M.A., Moresi, L.N. & Capitanio, F.A., 2014. Overriding plate controls on subduction evolution, *J. geophys. Res.,* **119,** doi:10.1002/2014JB011163.

Stegman, D.R., Freeman, J., Schellart, W.P., Moresi, L. & May, D.A., 2006. Influence of trench width on subduction hinge rates in 3-D models of slab rollback, *Geochem. Geophys. Geosyst.,* **7,** doi:10.1029/2005GC001056.

Stegman, D.R., Farrington, R., Capitanio, F.A. & Schellart, W.P., 2010. A regime diagram for subduction styles from 3-D numerical models of free subduction, *Tectonophysics,* **483,** 29–45.

Stevenson, D.J. & Turner, J.S., 1977. Angle of subduction, *Nature,* **270,** 334–336.

Strak, V. & Schellart, W.P., 2014. Evolution of 3-D subduction-induced mantle flow around lateral slab edges in analogue models of free subduction analysed by stereoscopic particle image velocimetry technique, *Earth planet. Sci. Lett.,* **403,** 368–379.

Tackley, P.J., 2000. Self-consistent generation of tectonic plates in time-dependent, three-dimensional mantle convection simulations, 1. Pseudoplastic yielding, *Geochem. Geophys. Geosyst.,* **1**(8), doi:10.1029/2000GC000036.

Tan, E., Gurnis, M. & Han, L., 2002. Slabs in the lower mantle and their modulation of plume formation, *Geochem. Geophys. Geosyst.,* **3,** doi:10.1029/2001GC000238.

Tovish, A., Schubert, G. & Luyendyk, B.P., 1978. Mantle flow pressure and the angle of subduction: non-newtonian corner flows, *J. geophys. Res.,* **83,** 5892–5898.

Uyeda, S. & Kanamori, H., 1979. Back-arc opening and the mode of subduction, *J. geophys. Res.,* **84,** 1049–1061.

van Dinther, Y., Morra, G., Funiciello, F. & Faccenna, C., 2010. Role of the overriding plate in the subduction process: insights from numerical models, *Tectonophysics,* **484,** 74–86.

Wessel, P., Smith, W. H.F., Scharroo, R., Luis, J. & Wobbe, F., 2013. Generic mapping tools: improved version released, *EOS, Trans. Am. geophys. Un.,* **94,** 409–410.

Williams, S., Flament, N., Muller, R.D. & Butterworth, N., 2015. Absolute plate motions since 130 Ma constrained by subduction zone kinematics, *Earth planet. Sci. Lett.,* **418,** doi:10.1016/j.epsl.2015.02.026.

Yamato, P., Husson, L., Braun, J., Loiselet, C. & Thieulot, C., 2009. Influence of surrounding plates on 3D subduction dynamics, *Geophys. Res. Lett.,* **36,** doi:10.1029/2008GL036942.

Zhong, S., 2006. Constraints on thermochemical convection of the mantle from plume heat flux, plume excess temperature and upper mantle temperature, *J. geophys. Res.,* **111,** doi:10.1029/2005JB003972.

Zhong, S. & Gurnis, M., 1995. Mantle convection with plates and mobile, faulted plate margins, *Science,* **267,** 838–843.

Zhong, S., Gurnis, M. & Moresi, L., 1998. Role of faults, nonlinear rheology, and viscosity structure in generating plates from instantaneous mantle flow models, *J. geophys. Res.,* **103,** 15 255–15 268.